Controls on the deep thermal field: implications from 3-D numerical simulations for the geothermal research site Groß Schönebeck

Yvonne Cherubini · Mauro Cacace ·
Magdalena Scheck-Wenderoth · Inga Moeck ·
Björn Lewerenz

Abstract The deep thermal field in sedimentary basins can be affected by convection, conduction or both resulting from the structural inventory, physical properties of geological layers and physical processes taking place therein. For geothermal energy extraction, the controlling factors of the deep thermal field need to be understood to delineate favorable drill sites and exploitation compartments. We use geologically based 3-D finite element simulations to figure out the geologic controls on the thermal field of the geothermal research site Groß Schönebeck located in the E part of the North German Basin. Its target reservoir consists of Permian Rotliegend clastics that compose the lower part of a succession of Late Carboniferous to Cenozoic sediments, subdivided into several aquifers and aquicludes. The sedimentary succession includes a layer of mobilized Upper Permian Zechstein salt which plays a special role for the thermal field due to its high thermal conductivity. Furthermore, the salt is impermeable and due to its rheology decouples the fault systems in the suprasalt units from subsalt layers. Conductive and coupled fluid and heat transport simulations are carried out to assess the relative impact of different heat transfer mechanisms on the temperature distribution. The measured temperatures in 7 wells are used for model validation and show a better fit with models considering fluid and heat transport than with a purely conductive model. Our results suggest that advective and convective heat transport are important heat transfer processes in the suprasalt sediments. In contrast, thermal conduction mainly controls the subsalt layers. With a third simulation, we investigate the influence of a major permeable and of three impermeable faults dissecting the subsalt target reservoir and compare the results to the coupled model where no faults are integrated. The permeable fault may have a local, strong impact on the thermal, pressure and velocity fields whereas the impermeable faults only cause deviations of the pressure field.

Keywords Thermal field · Coupled fluid and heat transport · Faults · Groß Schönebeck

Introduction

Geothermal energy production utilizes the Earth's internal heat and potentially provides a renewable energy resource which is increasingly exploited on a commercial scale especially to reduce CO_2 emissions. Hydrothermal energy systems utilize natural formation fluids brought to the surface through wells drilled for that purpose. Where the ratio of temperature and natural production rate is too low to generate energy, the geothermal system is enhanced by stimulation treatments. These anthropogenic geothermal systems are referred to as enhanced geothermal systems (EGS) typically developed by an injection and a production well to circulate thermal water (Huenges 2010). Any exploitation of geothermal energy, in particular from EGS resources, is affected by the temperature distribution in the subsurface that can vary regionally and over time. Different mechanisms of internal heat transfer—conduction, convection or both—control the temperature distribution of

Y. Cherubini
Institute of Earth and Environmental Science, University of Potsdam, Karl-Liebknecht-Str. 24-25, 14476 Potsdam, Germany

Y. Cherubini (✉) · M. Cacace · M. Scheck-Wenderoth ·
I. Moeck · B. Lewerenz
Helmholtz Centre Potsdam, GFZ German Research Centre for Geosciences, Telegrafenberg, 14473 Potsdam, Germany
e-mail: yvonne.cherubini@gfz-potsdam.de

the deep thermal field (Verhoogen 1980). The rate of heat and fluid flow is in turn affected by the composition of the geological layers (Bjørlykke 2010). Preferential pathways or tight barriers for fluids caused by faults and fractures may in addition significantly influence the fluid circulation and thermal field within the reservoir rocks. Therefore, it is important to investigate the processes that control heat transport in the subsurface. Numerical simulations enable studying the processes over time, taking place in geothermal systems and are, therefore, useful tools for both geothermal exploration and reservoir engineering, as they can provide necessary information on temperature variations and fluid circulation in greater depths. The positive aspect of numerical simulations is that they incorporate both, the structural setting of the subsurface and the physical processes of coupled fluid and heat transport. With this study, we investigate the geological controls on the deep thermal field by means of 3-D simulations in the vicinity of the hydrothermal EGS research site Groß Schönebeck, located 40 km north of Berlin in the North German Basin (Fig. 1).

The site is an in situ laboratory exhibited by a well-doublet system with one well (EGrSk 3/90) initially drilled for gas exploration and now acting as an injector (Huenges et al. 2002; Moeck et al. 2005). The second well (GtGrSk 4/05) has been drilled as a production well to establish a thermal water loop (Zimmermann et al. 2007). The in situ laboratory recently has been the target of an increasing number of studies aiming at improving its productivity (Blöcher et al. 2010; Huenges et al. 2006; Reinicke et al. 2005; Zimmermann et al. 2010, 2011).

Within the sedimentary succession of the Groß Schönebeck model area, a layer of mobilized Upper Permian Zechstein salt (Fig. 2a) plays a special role for the thermal field due to its high thermal conductivity and its special configuration. Previous modeling studies on

different scales already demonstrated that the different thickness of this salt rock, ranging from few tens of meters to more than several thousand meters, caused by salt tectonics, strongly control the thermal regime in the North German Basin (Bayer et al. 1997; Cacace et al. 2010; Kaiser et al. 2011; Noack et al. 2010; Scheck 1997). Besides, the sedimentary succession is decoupled into different aquifer systems by several hydrogeological barriers controlling most of the fluid flow in the subsurface. These hydrogeological barriers comprise the Tertiary Rupelian clays, the Triassic Muschelkalk limestones and the Zechstein salt. Due to its specific rheology, the latter also decouples the deformation pattern in the study area into a supra- and a subsalt compartment with specific fault systems each (Fig. 2b).

The thermal field of the Groß Schönebeck area has been recently investigated by Ollinger et al. (2010). Their 3-D conductive model indicated a thermal regime controlled by heat conduction and spatially variable thermal conductivities in the different geologic layers. Also, the cycle performance of the well-doublet system was evaluated by means of a thermohaline finite element simulation including deviated wells and hydraulically induced fractures in the reservoir zone of Groß Schönebeck (Blöcher et al. 2010). However, the thermal regime of the larger area around Groß Schönebeck and the influence of the natural fault zones have not been addressed up to now.

The present study investigates the controlling factors of the deep thermal field for the larger area of Groß Schönebeck by means of 3-D finite element simulations. Conductive and coupled fluid and heat transport simulations are carried out to assess the relative impact of different heat transfer mechanisms on the temperature distribution with respect to the hydrogeological setting in the study area. Furthermore, the influence of faults affecting the Lower Permian (Rotliegend) geothermal target

Fig. 1 **a** Map of Germany showing the location the Groß Schönebeck test site. The study area (*red rectangle*) covers a surface of 50 km in N–S and of 55 km in E–W direction.
b Topography map of the model area in UTM zone 33 N with main rivers and lakes (*thin black lines*) (ETOPO1, after Amante and Eakins 2009). The well GrSk 3/90 (*black dot*) indicates the position of the hydrothermal EGS research site Groß Schönebeck
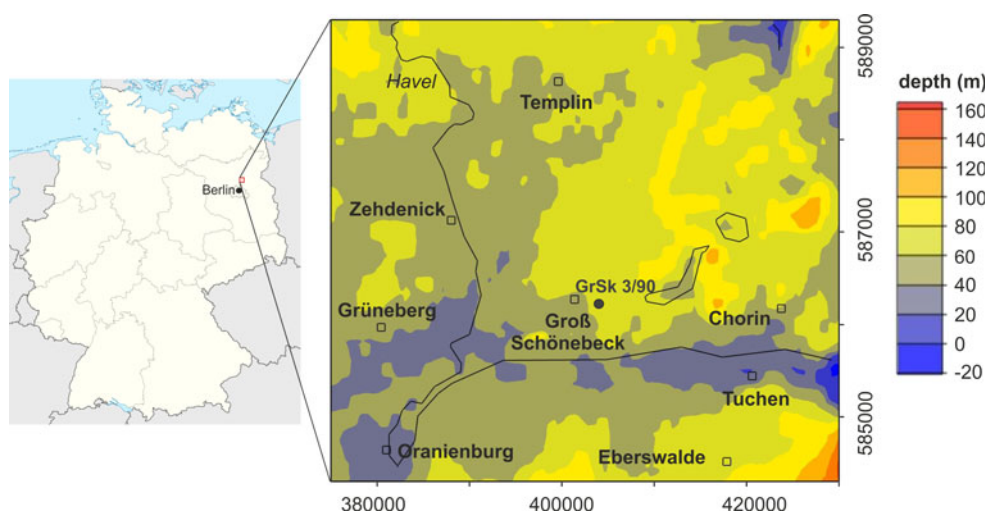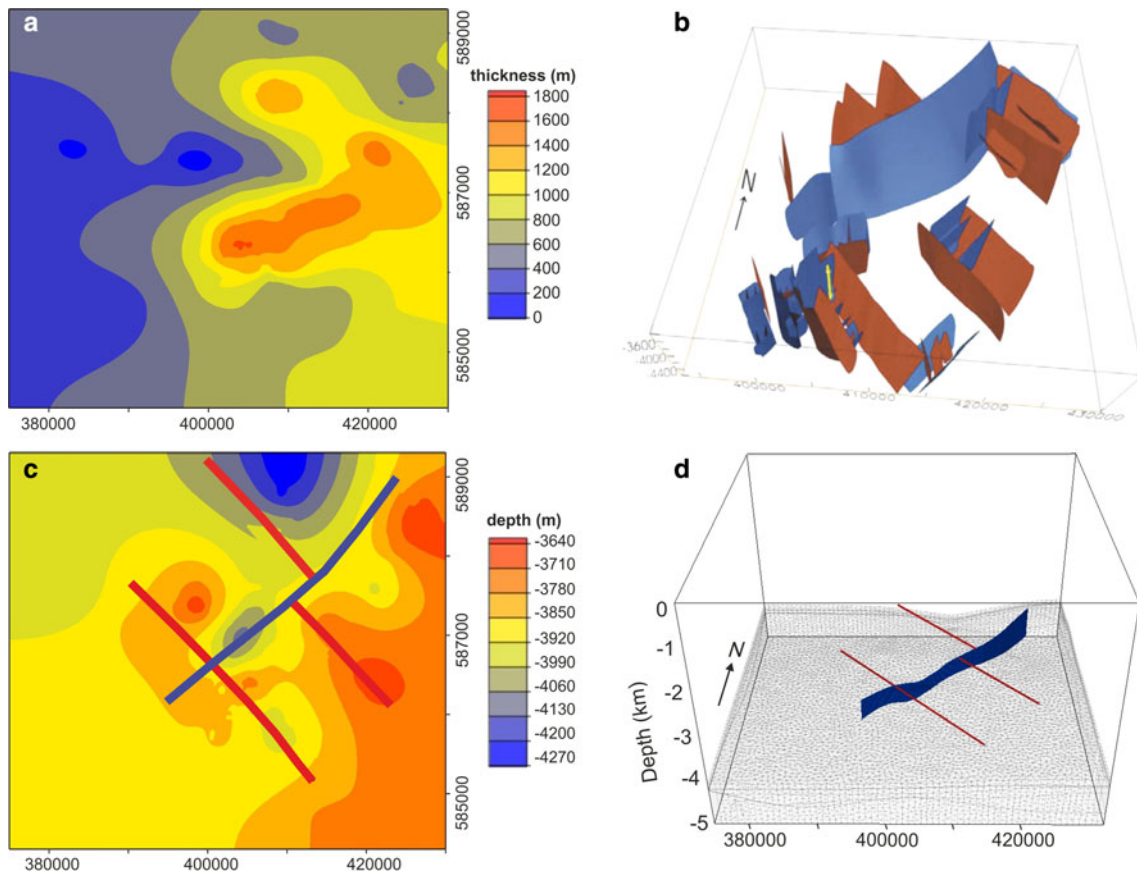
Fig. 2 a Thickness map of Permian Zechstein salt which is characterized by a two NE and NW trending salt ridges in the centre and NE. b 3-D hydrotectonic model for the Rotliegend reservoir indicating the hydraulic conductivity of the faults with respect to their kinematic behavior within the current in situ stress field (from Moeck et al. 2005). *Red faults* acting as seals; *blue faults* serving as conduits; *yellow tube* location of the well GrSk 3/90. Simplified subsalt fault

system representing the major faults in the area Groß Schönebeck at: c the Top Rotliegend depth map corresponding to the uppermost surface cut by the faults and d the implemented faults in the subsalt layers of the 3-D finite element model. According to b, in both subfigures the *red* NW–SE oriented faults are supposed to act as barriers, the *blue* NE–SW trending fault as a conduit to fluid flow

reservoir is studied by integrating major faults of the sub-salt fault system into the numerical model (Fig. 2c). The simulation results for the fault model are compared to a scenario where no faults are integrated to quantify the influence of the faults on the temperature and pressure fields and to assess the relevance of theses changes. To validate the models, calculated temperatures of all models are compared with corrected temperatures derived from wells located in the study area (Fig. 3a).

Geological setting and model setup

The structural model of the Groß Schönebeck area covers a surface of 50 km in N–S and of 55 km in E–W direction. It reaches down to −5 km depth and resolves a succession of Carboniferous to Quaternary age (Fig. 3a; Table 1). The Permain Zechstein salt layer subdivides the sedimentary succession into a supra and a subsalt sequence. The

dominating structure of the Zechstein is a NE–SW trending salt ridge (rising from ∼ −4,180 to −2,160 m) which has been formed by halokinetic processes (Fig. 2a).

The 3-D model of the Groß Schönebeck area used in this study is based on an earlier structural model (Moeck et al. 2005) that has been now vertically refined by integrating additional layers. This refinement allows differentiating the major hydraulically active layers in the suprasalt succession. Accordingly, the Cenozoic is differentiated into a Quaternary unit and Tertiary units. The Quaternary unit is mainly composed of unconsolidated, clastic sediments and its geometry corresponds to the 3-D structural model of Brandenburg in NE Germany (Noack et al. 2010). Deep reaching channels formed by subglacial erosion characterize the structural pattern of the base Quaternary, and are often filled with a variety of porous and permeable sediments (BURVAL Working Group 2009). The underlying Tertiary is composed of unconsolidated sands, silts, clay and marly limestones and is subdivided
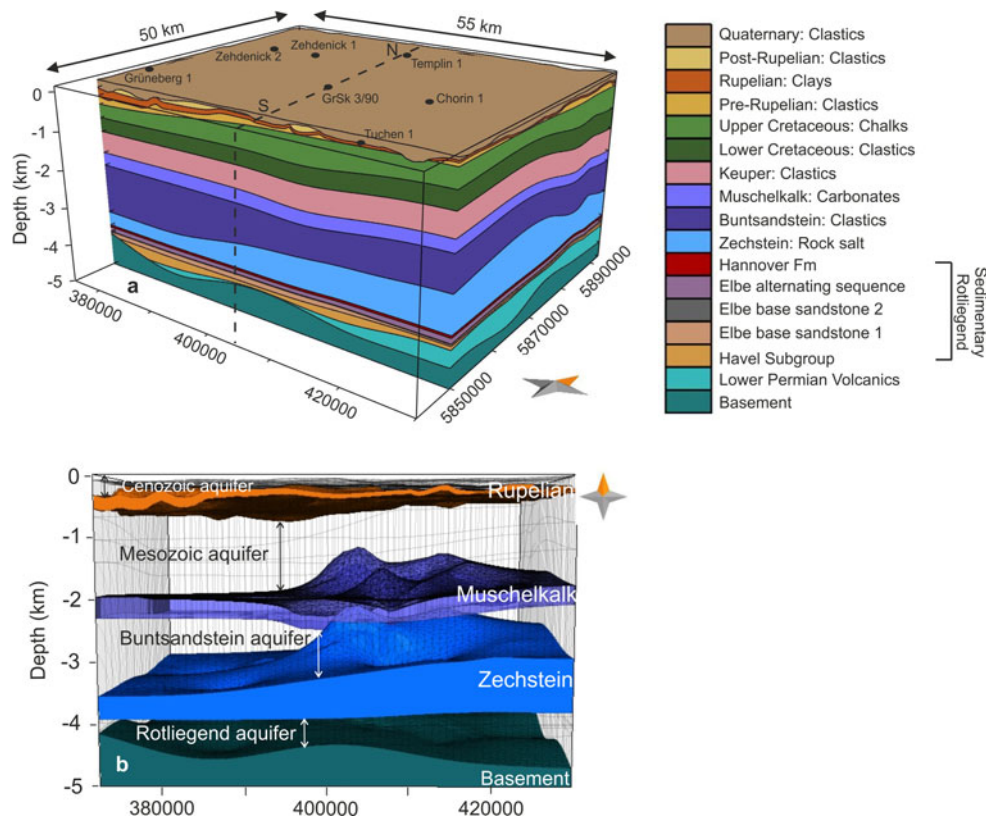
Fig. 3 a 3-D geological model of Groß Schönebeck with the stratigraphic layers (vertical exaggeration: 7:1). *Black points on top* indicate the location of the wells in the area Groß Schönebeck for which temperature measurements are available. The *dotted black line* delineates the location of the vertical cross section from N to S through the research well GrSk 3/90 used to illustrate results in Figs. 5, 7, and 8. The *frontal view* displays a vertical profile from W to E through well Tuchen 1. Note the Quaternary channel cutting the Upper Cretaceous layer at shallow depth (up to ∼200 m) in the SE.

b Distribution of low permeability aquicludes and high permeability aquifers integrated into the model (vertical exaggeration: 7:1). The quasi-impervious layers are from *bottom* to *top* (with average thickness in *brackets*): basement (540 m), Permian Zechstein (700 m), Triassic Muschelkalk (300 m), Oligocene Rupelian (120 m). The aquifer systems from *bottom* to *top*: Rotliegend aquifer (580 m), Buntsandstein aquifer (940 m), Mesozoic aquifer (1,770 m), Cenozoic aquifer (190 m)

into three sub-units—the Post-Rupelian, Rupelian and Pre-Rupelian. Of particular hydrogeological interest is the Oligocene Rupelian, mainly composed of clay. A low permeability characterizes this clay unit due to small grain sizes and a highly absorptive capacity. The Rupelian acts as the uppermost hydraulic barrier in the model separating the permeable geological units above (Quaternary and Post-Rupelian) and below (Pre-Rupelian and Mesozoic) (Table 1; Fig. 3b). The spatial distribution of the Rupelian layer is derived from well data provided by the Geological Survey of Brandenburg and adjusted to the geological maps available for the study area (Stackebrandt and Manhenke 2002).

Below the Tertiary, a succession of moderately consolidated marls, sand-, silt- and mudstones of Cretaceous to Jurassic age follows downward. As these stratigraphic horizons are characterized by similar physical properties, they are combined to a single layer of uniform properties in the model (Table 1). Following downward, the Upper and

Lower-Middle Keuper (Upper Triassic) formations are likewise merged into one single layer in the model, representing a uniform parameter domain, mainly composed of clays, marls and gypsum. Accordingly, this unit is less permeable than the overlying one.

In a similar way, the Upper–Middle Muschelkalk and Lower Muschelkalk (Middle Triassic) are assembled to form a single Triassic Muschelkalk layer. This stratigraphic unit consists of limestones and calcareous marls and this special lithology leads to a strongly reduced hydraulic activity. Accordingly, the Muschelkalk represents the second hydraulic barrier within the sedimentary succession (Fig. 3b).

Sediments like silts with minor sand partition, clays and evaporites are characteristic for the Lower Triassic Buntsandstein unit which is characterized by a moderate permeability. Following downward, the Upper Permian is considered as one layer predominantly composed of evaporates (mainly salt). Due to its specific mineral lattice

Table 1 Stratigraphic units with predominant lithologies and corresponding physical properties used for the numerical simulations of the geothermal field for the Groß Schönebeck area

Stratigraphic unit (predominant lithologies)	Permeability κ(m^2)	Porosity ε (%)	Rock heat capacity c^s (MJ/m^3 K)	Thermal conductivity (Wm^{-1} K^{-1})	Radiogenic heat production (10^{-7} W m^3)
Quaternary (sand, silts)	1.0E−12 (1.0E−12)	23 (23)	3.15 (3.15)	1.5 (1.5)	7 (9)
Post-Rupelian (sand, silts, clay)	1.0E−13 (1.0E−13)	23 (23)	3.15 (3.15)	1.5 (1.5)	7 (9)
Rupelian (clays)	1.0E−15 (1.0E−15)	20 (20)	3.3 (3.3)	1.0 (1.0)	4.5 (4.5)
Pre-Rupelian (sands, silts, marls)	1.0E−13 (1.0E−13)	10 (10)	2.4 (2.4)	1.9 (1.9)	3 (6)
Upper Cretaceous (marls, sandstones, siltstones)	1.0E−13 (1.0E−13)	10 (10)	2.4 (2.4)	1.9 (1.9)	3 (6)
Jurassic: Lower Cretaceous (siltstones, mudstones)	1.0E−13 (1.0E−13)	13 (13)	3.19 (3.19)	2 (2)	14 (15)
Keuper (clays, marls, gypsum)	1.0E−14 (1.0E−14)	6 (6)	3.19 (3.19)	2.3 (2.3)	14 (16)
Muschelkalk (limestones, marls)	1.0E−18 (1.0E−18)	0.1 (0.1)	2.4 (2.4)	1.85 (1.85)	3 (10)
Buntsandstein (silts, sands, evaporites)	1.0E−14 (1.0E−14)	4 (4)	3.15 (3.15)	2.0 (2.0)	10 (18)
Upper Permian Zechstein (evaporites, mainly salt)	Impermeable ∼0 (∼0)	∼0 (∼0)	1.81 (1.81)	3.5 (4.5)	0.9 (4)
Upper Rotliegend: Hannover Fm (sandstones, mudstones, siltstones)	1.0E−14 (1.0E−16)	3 (1)	2.67 (2.4)	1.84 (1.9)	10 (18)
Upper Rotliegend: Elbe alternating sequence (sandstones)	1.0E−14 (1.61E−15)	3 (3)	2.67 (2.4)	1.84 (1.9)	10 (14)
Upper Rotliegend: Elbe base sandstone 2 (sandstones)	1.0E−14 (6.44E−14)	3 (8)	2.67 (2.4)	1.84 (2.9)	10 (14)
Upper Rotliegend: Elbe base sandstone 1 (sandstones)	1.0E−14 (1.29E−14)	3 (15)	2.67 (2.4)	1.84 (2.8)	10 (10)
Upper Rotliegend: Havel Subgroup (sandstones, conglomerates)	1.0E−14 (2.58E−16)	3 (0.1)	2.67 (2.6)	2.13 (3.0)	10 (12)
Lower Permian Volcanics (andesites, rhyolithes)	1.0E−14 (3.22E−16)	3 (0.5)	2.67 (3.6)	2.5 (2.3)	20 (10)
Carboniferous (basement rocks)	Impermeable ∼0 (∼0)	∼0 (∼0)	2.46 (2.7)	2.65 (2.7)	15 (20)

Hydrogeological barriers separating the stratigraphic succession into different aquifer systems are highlighted (bold)

Permeabilities, porosities and heat capacities assigned after Magri (2005)

Permeability, porosity and heat capacity values for Post-Rupelian, Rupelian, Pre-Rupelian after Magri et al. (2008)

Thermal conductivities and radiogenic heat production after Scheck (1997). Thermal properties for Post-Rupelian, Rupelian, Pre-Rupelian adapted from Magri et al. (2008). Radiogenic heat production value for the Rupelian after Balling et al. (1981)

In brackets another set of properties tested in the numerical simulations. Permeabilities, porosities and heat capacities for the Cenozoic to the Upper Permian Zechstein and for the Carboniferous after Magri (2005; Scheck 1997); for the Upper Rotliegend Formation to Late Carboniferous after Blöcher et al. 2010; for Post-Rupelian, Rupelian, Pre-Rupelian after Magri et al. (2008)

Thermal conductivities and radiogenic heat production for the Cenozoic to Upper Permian Zechstein after Norden and Förster (2006) and Norden et al. (2008); for Post-Rupelian, Rupelian, Pre-Rupelian after Magri et al. (2008). Radiogenic heat production for the Rupelian after Balling et al. (1981). Thermal conductivities for the Upper Rotliegend Formation to Late Carboniferous after Blöcher et al. 2010, for Carboniferous after Ollinger et al. 2009

and its mechanical properties, the porosity and permeability of the salt are extremely low (cf. Hudec and Jackson 2007). Consequently, the Zechstein salt is considered as hydraulically impermeable and acts as the third hydraulic barrier in our model (Fig. 3b). Moreover, the salt is thermally more conductive than other sediments.

The subsalt sequence includes the Permian Rotliegend deposits, corresponding to the Rotliegend aquifer, and a layer of uppermost Carboniferous. The first represents the target reservoir zone of the geothermal site (Zimmermann

et al. 2007). The deposits of the Upper Rotliegend are subdivided into the Hannover Formation with mainly mudstones and fine-grained sandstones and the Dethlingen Formation, which is composed of fine- to coarse-grained sandstones. At the base of the Upper Rotliegend, sandstones and clast-supported conglomerates form the Havel Subgroup (Holl et al. 2005). The Lower Rotliegend consists of volcanic (andesitic) rocks. Foliated, flyschoid sediments form the Carboniferous rocks integrated in the model as the lowermost impermeable layer.

Summarizing, the final structural model as used in the simulations consists of 17 geological layers (Fig. 3a) with a horizontal resolution of 220 m × 227 m. The three hydrogeological barriers—the Rupelian, the Muschelkalk and the Zechstein—separate the stratigraphic succession of the model into different aquifer systems (Fig. 3b). Accordingly, four main aquifer systems can be distinguished from top to bottom: (1) the Cenozoic aquifer (from surface to Post-Rupelian); (2) the 'Mesozoic' aquifer (between Rupelian and Muschelkalk); (3) the Buntsandstein aquifer (between Muschelkalk and Zechstein); and (4) the Rotliegend reservoir (between Zechstein and Carboniferous basement).

Fault system

Seismic data image a fault pattern in the study area which is mechanically decoupled by the Zechstein salt into a suprasalt and a subsalt fault system (Moeck et al. 2009). Due to the impermeability of the salt layer, the different fault systems are hydraulically isolated where the salt rock reaches a thickness of tens to thousands of meters. This decoupling allows a separate consideration of the behavior of the two systems.

The suprasalt structure is dominated by the Zechstein morphology of NE–SW trending salt ridges and surrounded by salt rim synclines (Moeck et al. 2009). Major NW–SE and minor NE–SW oriented faults dominate the subsalt fault system in the Rotliegend rocks (Fig. 2b). Displacement along the faults indicates normal faulting by hanging wall down movement (Moeck et al. 2009).

A stress regime between normal faulting and a transition to strike-slip faulting is indicated in the Groß Schönebeck Rotliegend reservoir by an integrated approach of 3-D structural modeling, 3-D fault mapping, stress ratio definition based on frictional constraints, and a slip-tendency analysis (Moeck et al. 2009). Faults with high shear stress are supposed to be hydraulically active (e.g. Ito and Zoback 2000; Zhang et al. 2002, 2007) and extensional faults may act as fluid-conduits (e.g. Gudmundsson et al. 2002). Therefore, the discrimination of critically stressed faults and extensional faults within the current stress field allows assessing the hydraulic conductivity of faults in the geothermal aquifer, by resolving the amount of shear stress and normal stress on any fault plane (by slip-tendency analysis) (Moeck et al. 2009). Arising thereby, the NNE to NE trending moderately dipping faults bear the highest shear stresses in response to the current stress field and as critically stressed faults, they are supposed to act as preferential pathways for fluid flow (Barton et al. 1995; Moeck et al. 2009). By contrast, the non-critically stressed NW–SE trending faults are expected to serve as barriers to fluid flow (Fig. 2b).

As only the subsalt fault system affects the reservoir target zone, we integrate only the latter into the model. Therefore,

the fault pattern is simplified, in that the major faults are integrated as representative fault zones, dissecting the Rotliegend reservoir, from top Hannover Formation to top Basement (Fig. 2c). According to their hydraulic conductivity with respect to the current in situ stress field (Fig. 2b), a major NE–SW trending fault, which has been interpreted from seismic sections (Moeck et al. 2009), is supposed to act as a conduit and three minor NW–SE oriented faults are considered as barriers to fluid flow (Fig. 2c, d).

Methods

The coupled fluid and heat transport models are based on the finite element method (FEM) and the simulations are carried out with the commercial software FEFLOW® (Diersch 2002). FEFLOW® is a software package for modeling fluid flow and transport processes in porous media with variable fluid density effects. The governing partial differential equations of density coupled thermal convection in saturated porous media are based on Darcy's law, as well as on mass and energy conservation laws (e.g. Bear 1991; Nield and Bejan 2006). The description of the equations is given in the "Appendix".

FEM model construction: spatial discretization and parametrization

As a first step, the geometry of the stratigraphic layers as derived from the structural model described above is transferred into a format applicable for its use in a numerical simulation.

In general, the basic algorithms provided by the software FEFLOW® are two and a half dimensional. A 3-D model is generated by vertical superposition of 2-D unstructured triangular surfaces, representing internal geological boundaries (i.e. slices of the 3-D model). All slices share the same horizontal spatial discretization. The third dimension is entered by vertically connecting nodal points between two confining slices to form a layer of the 3-D model. Therefore, the starting point for the finite element model generation is to define a "supermesh" in FEFLOW® which forms the framework for the generation of the finite element mesh and contains all basic geometrical information the mesh generation algorithm needs (Diersch 2002). By means of this 2-D planar geometric object, the outer boundary of the model area is defined. Furthermore, lines representing the geometry of the faults' traces (Fig. 2c) are inserted within the supermesh prior to the triangulation phase. By adding those piecewise linear polylines as internal constraints to the triangulation, the trace of the fault could be fully restored within the model. Based on the geometric frame provided by the supermesh,

a 2-D unstructured triangle mesh is generated. In order to best approximate discrete faults as well as to enforce numerical stability for the simulation, a higher order of element refinement along the fault lines is performed than in the remaining part of the model.

To reproduce the geological structure, the z-coordinates of each geological top and base surface are assigned to each node of the corresponding top and bottom slice. Therefore, the resulting layer thicknesses a priori determine the vertical resolution of the numerical model. To optimize the numerical stability, the vertical resolution of the model is enhanced by subdividing two layers of large thicknesses (the Lower Triassic Buntsandstein and the Permian Zechstein) into two sub-layers of equal thicknesses, respectively. A planar slice at a constant depth of −5,000 m is integrated, along the base of the model to enforce numerical stability.

The major NE–SW oriented fault (conduit, Fig. 2c, d) is implemented by means of discrete feature elements. The latter represent finite elements of lower dimensionality, which can be inserted at element edges and faces (Diersch 2002). In principle, FEFLOW® offers several distinct laws of fluid motion for discrete feature elements: Darcy, Hagen-Poiseuille and Manning-Strickler. Here, we use vertical 2-D discrete elements and assume Darcy's law to describe fluid flow within the fault. The minor NW–SE trending faults (barriers, Fig. 2c, d) are modeled as equivalent porous media. They are represented by finite element areas for which a very low permeability is assigned along the trace of the fault. The respective areas of mesh refinement are set for 20 m on either side of the faults traces (lateral extent in total 40 m per fault barrier). The final 3-D finite element model is composed of 20 slices and accordingly 19 layers. The model consists of approximately five million elements (=triangular prisms).

According to the main lithology of each geological unit, hydraulic and thermal rock properties are assigned constant to each corresponding layer in the numerical model (Table 1) and to the fault (Table 2). Each layer is considered homogenous and isotropic with respect to its physical properties. Taking into account anisotropic conditions would increase the understanding of the already complex interaction between physical processes and the composition of geological layers, but should be considered in future research as soon as detailed data are available.

Generally, the thermal conductivities increase downward due to compaction. An exception is the high thermal conductivity of the Zechstein salt layer.

Simulations

An overview of all simulations is given in Table 3. To evaluate the influence of the dynamic coupling between heat and fluid transport processes, an uncoupled simulation is carried out, in which only the conductive heat transfer is considered (model 1). Within model 2, in addition to the conductive heat transport, the movement of fluid is allowed and fluid density effects are taken into account, resulting in a coupled fluid and heat transport simulation.

To assess the impact of faults on the coupled fluid and heat system, faults are implemented in model 3. The simulation results are compared with model 2, in which no fault is included.

Time discretization

The uncoupled model 1 is performed as a steady-state simulation assuming equilibrium conditions for the conductive heat transfer. The transient coupled fluid flow and heat transport simulations for the models 2 and 3 are carried out for 250,000 years to obtain steady-state conditions. All results are shown for the final simulation state at 250,000 years.

Boundary and initial conditions

For the top flow boundary condition, a fixed hydraulic head equal to the topographic elevation is set. Thereby, the groundwater flow is mainly controlled by gradients in the topography. At the model base, a no-flow boundary condition is assigned to simulate the impermeable nature of the basement.

For the temperature boundary conditions, a fixed constant surface temperature of 8 °C is assumed, representing the average surface temperature in NE Germany (Katzung 1984). At the model base, a basal heat flux Q (mW/m²) is prescribed that allows a variable temperature distribution in −5 km depth (Fig. 4). The spatially varying heat flux for the modeled area is extracted from a lithosphere-scale conductive thermal model of Brandenburg (Noack et al. 2012). This model takes into account the thermal effects of the underlying differentiated crust and lithosphere, down to a depth of −125 km.

The pressure and temperature initial conditions are obtained from steady state uncoupled flow and heat transport simulations.

Results

Conductive model 1

The preliminary investigation of the purely conductive model (1) permits a later comparison with the coupled fluid and heat transport model (2), and allows a clear distinction between conductive heat transfer mechanisms and coupled components. Conductive heat transfer occurs due to rock

Table 2 Table with physical properties assigned for the faults

| Property	Fault$_{Conduit}$	Fault$_{Barrier}$
Porosity φ	0.3	~ 0
Heat capacity c^s (MJ/m^3 K)	2	2.67
Thermal conductivity (W m^{-1} C^{-1})	2	1.84
Permeability κ (m^2)	1E−09	Impermeable ~ 0
Radiogenic heat production (10^{-7} W m^3)	8	10

Porosity, heat capacity, thermal conductivity, radiogenic heat production values for the conduit represent average values of the geological layers (adopted from Bächler et al. 2003; Clauser and Villinger 1990), whereas for the barriers the same values as for the Sedimentary Rotliegend are used

Table 3 List of all simulations presented

Models	Type of simulation
(No fault) models	
1	Steady-state conductive
2	Transient coupled fluid and heat transport
Fault model	
3	Transient coupled fluid and heat transport

molecules transmitting their kinetic energy by collision (Turcotte and Schubert 2002). Figure 5a displays a representative, geological cross section, vertically cutting the model from north to south. The position of the cross section is sketched in the geological model in Fig. 3a and cuts the location of the Groß Schönebeck well GrSk 3/90. The profile dissects two major salt pillows in the central and in the northern part of the cross section, bordered by salt rim synclines. Figure 5b shows the corresponding temperature distribution along the cross section for the conductive model 1. The temperature pattern above the Zechstein salt is characterized by almost flat isotherms which reflect the diffusive nature of heat transfer via conduction. Only directly above the major salt pillows, in particular above the thick pillow in the central part, the isotherms are slightly bent convex upward.

Throughout the Zechstein salt, the temperature pattern is disturbed showing isotherms which are bent convex downward within the two major salt pillows. In the area of the salt rim synclines the isotherms are bent convex upward. This temperature pattern gives rise to a dipole-shaped thermal anomaly above and within major salt structures. This thermal anomaly is induced by thermal refraction, as triggered by the sharp contrast in thermal conductivity between the thermally more conductive salt and the less conductive surrounding sediments (Table 1).
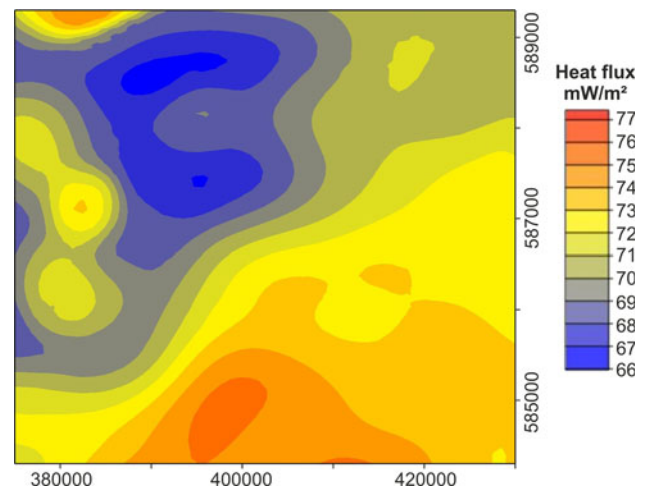
Fig. 4 Spatially varying heat flux used as lower thermal boundary condition extracted from a lithosphere-scale conductive thermal model of Brandenburg (Noack et al. 2012)

The temperature pattern observed within the Zechstein salt continues downward throughout the entire pre-salt sequence: below the major salt pillows we find convex downward shaped isotherms indicating cooler temperatures. By contrast, the isotherms are bent convex upward below the salt rim synclines reflecting increased temperatures.

According to Fourier's law, the energy flow is equal to the thermal conductivity multiplied by the temperature gradient within the rock. Increasing the rock thermal conductivity enhances the energy flow within the system. Therefore, the high thermal conductivity of the salt exerts a strong control on the entire conductive temperature field. This phenomenon is known as the "chimney effect" (cf. Scheck 1997). Accordingly, salt structures act as chimneys of efficient heat transfer and thus cause higher temperatures above salt structures and lower temperatures in and below the two major salt pillows (Fig. 5b).

The higher temperatures in the area of the salt rim synclines are mainly induced by the sediments overlying the salt. Due to their low thermal conductivities, they cause heat storage, i.e. thermal blanketing.

Comparsion between modeled and measured temperatures

For validation of our simulation results, the modeled temperatures are compared to observed temperatures from different wells in the vicinity of Groß Schönebeck (Tables 4, 5). Observed temperature values available for the different wells are plotted against depth in comparison with the modeled temperature gradients for the respective well (Fig. 6a–g).
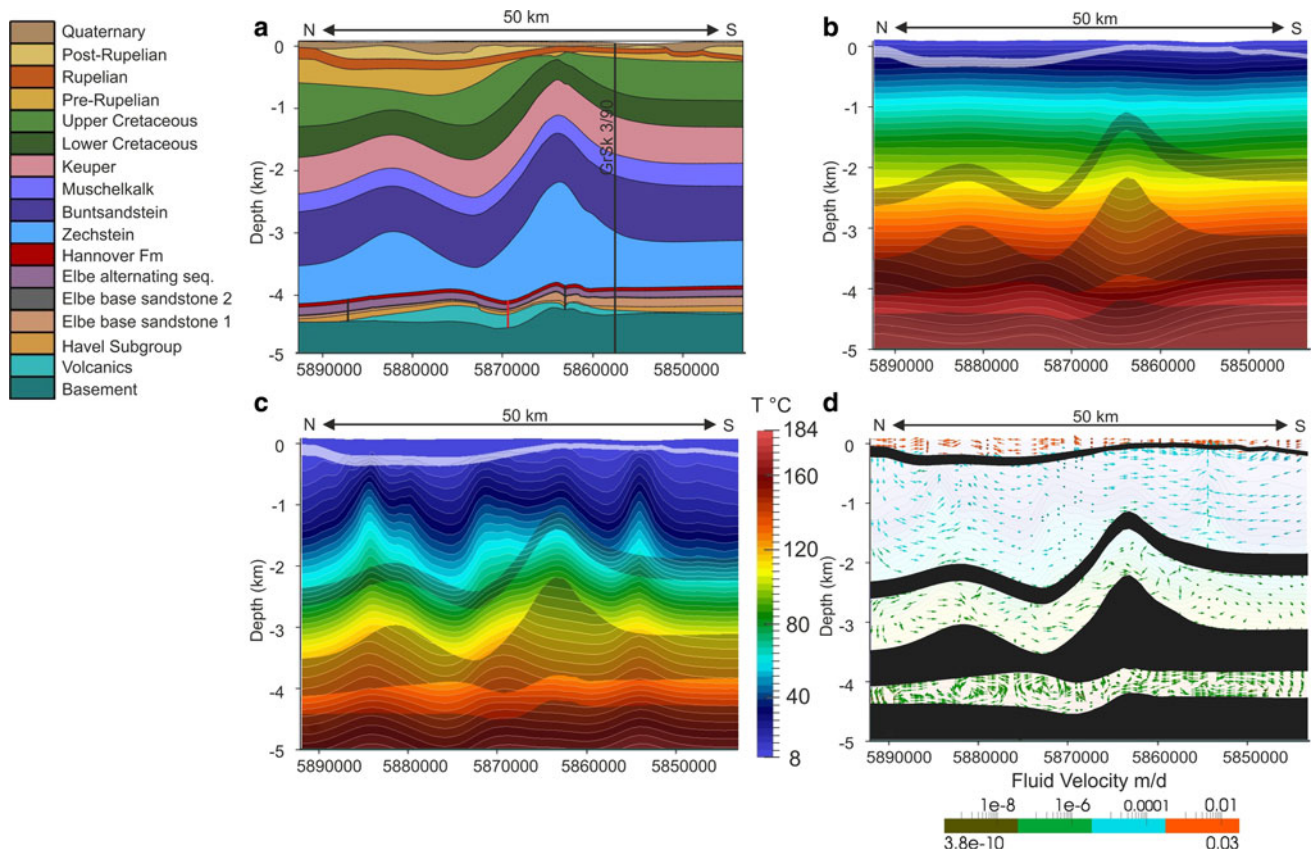
Fig. 5 a Vertical geological cross section from N to S through GrSk 3/90 for which the results in **b**, **c**, **d** and Figs. 7 and 8 are shown. Position of the well is displayed by the *black solid line*. The location of the cross section is delineated in Fig. 3a by the *dotted black line*. The location of the permeable fault cutting the central part of the cross section below the salt rim syncline is indicated by the *red solid line*. The positions of the two fault barriers dissecting the profile in the N and S parts are displayed by *black solid lines*. The outlines of the quasi-impervious Basement, Zechstein and Muschelkalk layers are *gray-shaded* and Ruplian is *white-shaded* in the background of the temperature profiles of **b**, **c** and Fig. 7a. In **d** and Fig. 7c, these four layers are *black-shaded*. Vertical exaggeration: 7:1 for all sections. **b** Temperature distribution of the conductive model 1. The conductive thermal field is generally characterized by flat isotherms, which are locally bent in response to the highly conductive Zechstein salt. **c** Temperature distribution of the coupled fluid and heat transport model 2. Fluid flow processes alter the thermal regime as displayed by the convex up- and downward shaped isotherms. The development of the coupled fluid system and thermal field is closely related to the distribution of permeable and impermeable sedimentary layers. **d** Combination plot of the fluid velocity vectors (length non-scaled) and temperature distribution with reduced intensity in the background. The vectors illustrate the different fluid flow characteristics and changing velocities in the four aquifer systems decoupled from each other

The comparison of the well measurements (black rhombs) with the modeled temperatures of the conductive model 1 (red solid line) shows that the temperatures predicted by the conductive model are too hot (mean value of $\Delta T = 11$ K), except for well location Chorin 1/71 where the well data show a very good fit with the modeled values (Fig. 6c). This well penetrates the slope of a thick NE–SW trending salt ridge (cf. Fig. 2a). Accordingly, the temperatures in well Chorin 1/71 are measured within the Zechstein (Ollinger et al. 2010), and directly below the salt. Consequently, predominant conductive heat transfer is expected in response to the hydraulic impermeability of the salt. Likewise, the simulated temperatures of the conductive model 1 reveal a good fit with the two uppermost observed temperatures at well GrSk 3/90 throughout the

Zechstein salt, also indicating heat transfer via conduction there (Fig. 6e). Except for Chorin 1/71 and the two uppermost observed temperatures at GrSk 3/90 (Fig. 6c, e), the modeled temperatures of the conductive model 1 do not reproduce the observations. The relatively large misfit between modeled and observed temperatures points toward other heat transfer processes that may influence the thermal field in addition to conduction.

Coupled fluid and heat transport model 2

Within model 2, we investigate the possible influence of fluid flow processes on the thermal field, as one possible additional mechanism. Fluid density driven convection and advection induced by topography-driven groundwater

Table 4 Observed temperatures in wells used for the comparison with modeled temperatures of the conductive model 1, the coupled fluid and heat transport model 2 and an additional simulation in which the permeability of the Rupelian clay is decreased to $k = 1E-18\ m^2$ (see "Discussion and conclusions")

Well	TD of log/ depth of BHT (m)	T at TD of log (°C)	$T_{corr.}$ at TD of log (°C)	T of conductive model 1 (°C)	T of coupled model 2 (°C)	T of additional coupled model (°C)
Chi/Chorin 1/71	3,800	144.3	147	144	111	112
Gür/ Grüneberg 2/74	4,100	157	161	172	152	160
Tl/Templin 1/95	1,652	69.3		87	55	58
Tuc/Tuchen 1/74	4,250	139.8	147	170	137	138
Zeh/ Zehdenick 2/75	3,650	139		160	138	138
Zeh/ Zehdenick 1/74	4,250	159.5	162	174	147	148

Temperature (T) at total depth (TD) of temperature log and corrected temperature ($T_{corr.}$) at TD of log for perturbed logs after Förster (2001)

Table 5 Observed temperatures in wells after Norden et al. (2008), used for the comparison with modeled temperatures of the conductive model 1, the coupled model 2 and an additional model in which the permeability of the Rupelian aquitard is decreased to $k = 1E-18\ m^2$ (see "Discussion and conclusions")

Well	Depth (m)	Temperature (°C)	Quality	T of conductive model 1 (°C)	T of coupled model 2 (°C)	T of additional coupled model (°C)
GrSk/Groß Schönebeck 3/90	2,800	119.9	Unperturbed	123	101	113
	3,770	135.1	Unperturbed	144	124	135
	4,230	148.6	Unperturbed	161	142	152
	4,286	150.8	Unperturbed	163	144	154
Chi/Chorin 1/71	2,900	126.6	Slightly perturbed	123	87	88
	3,650	139.8	Slightly perturbed	139	105	107

flow are both taken into account within the simulation. Figure 5c shows the temperature distribution and Figure 5d the velocity field of the coupled fluid and heat transport model 2 for the same geological cross section (Fig. 5a). Compared to the conductive model 1 (Fig. 5b), the isotherms are depressed, displaying distinctively lower temperatures (range ∼20–40 °C). This temperature drop is induced by the adopted upper thermal boundary conditions (8 °C) generating a permanent cold water inflow at the model surface with highest fluid velocities (0.001–0.03 m/day) (Fig. 5d). Except for the Cenozoic aquifer, the isotherms are not flat like in the conductive case (Fig. 5b).

In the suprasalt sequence, the isotherms are bent convex upward above thick salt rim synclines, bordered by convex downward shaped isotherms (Fig. 5c). The fluid vectors reflect the isotherm distribution and upward movement of the fluid is observed in areas where the isotherms are bent convex upward (Fig. 5d). Fluid velocities of 1E−5 to 1E−4 m/day occur within the Mesozoic aquifer and decrease within the Buntsandstein aquifer (∼1E−6 m/day). Within the latter, the thermal disturbances are also weaker than in the Mesozoic aquifer.

These thermal instabilities are characteristic for thermal density driven convective heat transport which is associated with the circulation of hot fluids. The heat is carried by the fluid movement, originating out of fluid density changes due to temperature variations: the heated fluid from the deeper regions becomes buoyant and rises due to its lower density, forming convection cells (Bundschuh and Arriaga 2010). Generally, the development of thermal convection is observed in permeable aquifers (Table 1; Fig. 3b). In these aquifers, the fluid is allowed to circulate in the free void space of the sediments (Fig. 5d). However, the
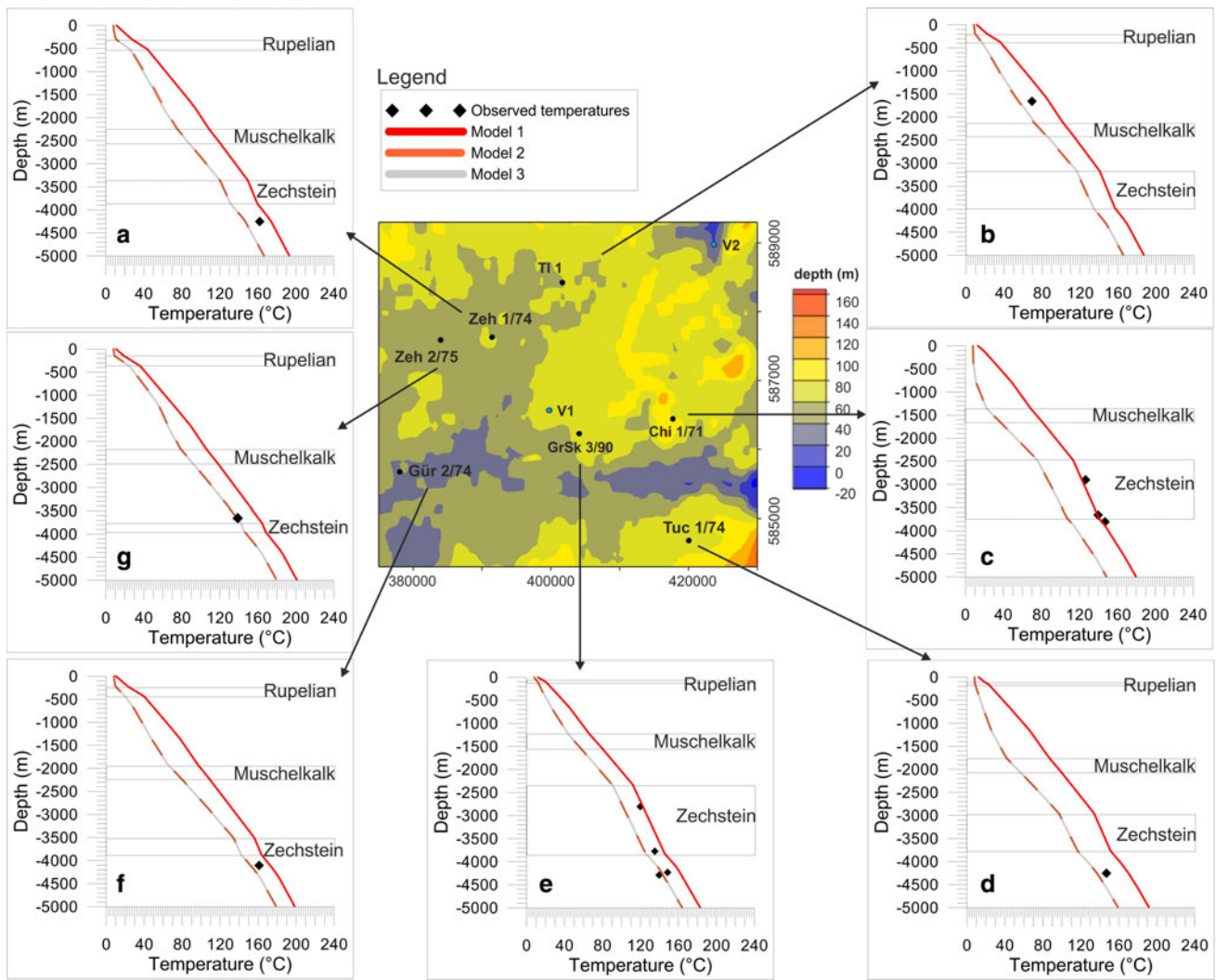
Fig. 6 Map of the surface topography (defining the hydraulic upper boundary condition) with the locations of the different wells. V1 and V2 display the positions of two virtual wells for which calculated temperatures-depth gradients are plotted in Fig. 11. **a–g** The observed temperature values available for the different wells are plotted against depth in comparison with the modeled temperature gradients for the respective well. Observed temperatures are displayed by *black rhombs*. The modeled temperatures for conductive model 1 are represented by *solid red lines*, for the coupled model 2 by *dotted orange lines* and for the fault model 3 by *solid gray lines*. The depth position of the Rupelian, the Muschelkalk and the Zechstein layers is outlined by *gray lines* in the background in each figure

development of pronounced convection cells is obviously favored by a larger thickness (cf. Bjørlykke 2010), which is only the case for the Mesozoic aquifer (Fig. 3b).

Hydraulically impermeable layers, like Zechstein, Muschelkalk and Rupelian, inhibit fluid movement and thus the progression of convection cells from one aquifer to another. Therefore, the extension of convective flow within the Mesozoic aquifer system is limited by the Muschelkalk and Rupelian aquicludes (Fig. 5c).

In the area of the Zechstein salt, convex upward and downward shaped isotherms above and below major salt pillows again reflect the chimney effect triggered by the high thermal conductivity of the salt (Fig. 5c).

Throughout the Rotliegend aquifer system, corrugated to flat isotherms are present. Although fluid circulation is observed within this less thick aquifer (Fig. 3b), the very low fluid velocities (3.8 to 1E−8 m/day) (Fig. 5d) and the flat character of the isotherms point to predominant conductive heat transfer within the aquifer.

However, compared to the conductive model 1, the convex upward shaped isotherms in and below the salt rim synclines are more pronounced. The increased temperatures are, like for the conductive case, due to thermal blanketing, caused by the thermally less conductive, thick post-salt sediments but also additionally triggered by the thermal feedback from the convection cells above. This

thermal feedback leads to a more pronounced isotherm deviation than in the conductive model 1 (Fig. 5b).

Comparison between modeled and measured temperatures

The comparison of the well measurements (black rhombs) with the modeled temperatures of the coupled model 2 (dotted orange line) reveals a good fit with the observed temperature values in Tuchen 1/74 (Fig. 6d), GrSk 3/90 (Fig. 6e), Grüneberg 2/74 (Fig. 6f), and Zehdenick 2/75 (Fig. 6g) (deviations < 10 K). In Zehdenick 1/74 (Fig. 6a) and Templin 1/95 (Fig. 6b), the temperature deviations are slightly higher (>10 °C). At these locations, the observed temperatures are located between the conductive (red solid line) and coupled (dotted orange line) model predictions which complicate a clear distinction between conductive and coupled heat transport processes. However, all modeled temperature curves for the coupled simulation show a very similar trend in each well. With increasing depths, the temperatures increase steadily though the values are smaller than in the conductive model 1 for the same depth. Only in the thickness ranges of the Rupelian, the Muschelkalk and the Zechstein layers, the slope of temperature curves is parallel to the conductive case, confirming the impermeable nature of these layers that hamper cold water inflow from the surface into deeper parts of the model. At locations, where the Rupelian is eroded (Chorin 1/71, Fig. 6c), strong cooling is observed in shallower depth levels (<−1,500 m) caused by the unhampered cold water inflow from the surface into the Mesozoic aquifer (Fig. 3b). The enhanced cooling in the shallow part of well location Tuchen 1/74 (Fig. 6d) can be explained by the presence of a quaternary channel in lateral offset of the well (Fig. 3a). The permeable subglacial channel hydraulically connects the Quaternary with the Mesozoic aquifer providing local pathways for the cold inflow from the surface.

In summary, the modeled temperatures of the coupled model 2 fit the observations better than the temperatures of the conductive model 1. These results suggest that the assumption of a coupled fluid and heat transport system approximates the natural temperature regime observed in the area Groß Schönebeck better than the purely conductive mechanism. Nevertheless, greater temperature deviations are still found between observations and model predictions. Generally, the temperatures of the coupled model 2 are colder than the measured values (Tables 4, 5). In Chorin 1/71, large deviations between measured and simulated temperatures of model 2 (33.3–38.6 K) are due to the predominant conductive heat transport throughout the Zechstein salt (Tables 4, 5). For the same reason, the uppermost temperature values of the coupled model 2 are too cold (11–18.9 K) compared to the observed

temperatures at well GrSk 3/90 throughout the Zechstein salt (Table 5). Also, the lowermost temperatures at GrSk 3/90 underestimate the observations (6.6–6.8 K, Table 5) as well as the values at Grüneberg 2/74 (5 K), Templin 1/95 (14.3 K), Tuchen 1/74 (2.8 K), Zehdenick 2/75 (1 K) and Zehdenick 1/74 (12.5 K) (Table 4). Possible reasons for these deviations could be the choice of physical properties assigned for the geological units, the structural limitations of the model and the choice of boundary conditions (see "Discussion and conclusions"). Another reason could be related to the impact of faults on the thermal field. To assess the potential influence of faults on the target reservoir of the Groß Schönebeck well (GrSk 3/90), we implemented the major faults in this reservoir into a third series of simulations.
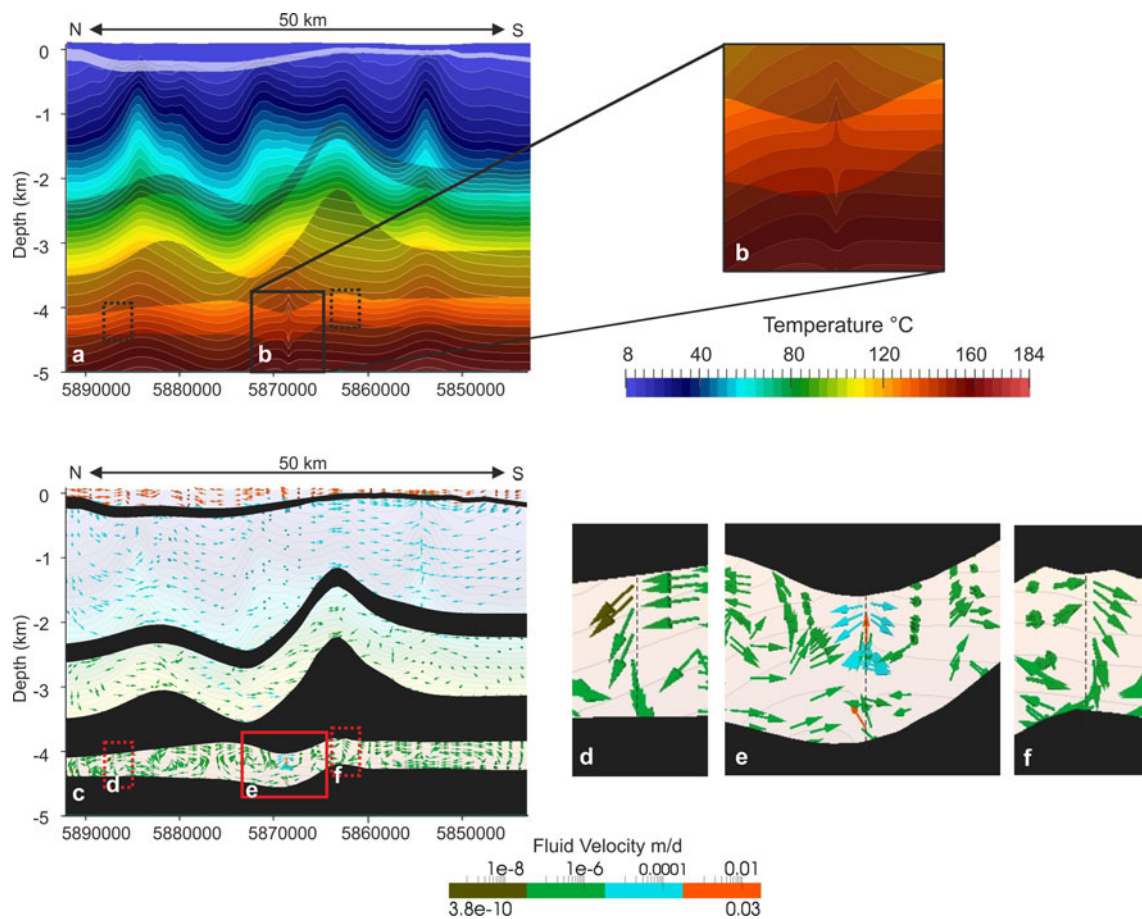
Fault model 3

Vertical cross section

In model 3, a major NE–SW oriented permeable fault and three NW–SE oriented impermeable faults are integrated (Fig. 2c, d). The simulation results of fault model 3 are compared with the coupled model 2, in which no faults are included (in the following referred to as no fault model 2). The results of fault model 3 are illustrated in Fig. 7a for the same vertical cross section as shown in Fig. 5a which is cut by three faults, including two barriers and one conduit.

The locations of the two fault barriers in the N and S parts of the cross section are framed by dotted black rectangles in Fig. 7a. By comparison to the no fault model 2 (Fig. 5c) and to the conductive model 1 (Fig. 5b), no differences can be traced in the isotherm pattern, indicating that the fault barriers have no remarkable influence on the thermal field. Due to their very low permeability and porosity (Table 2), they are almost impermeable and unable to conduct heat by fluid flow. Therefore, conductive heat transport is likely to persist as the predominant heat transfer mechanism in those areas. Because the thermal properties of the barriers do not differ from the rock matrix of the Sedimentary Rotliegend (Table 1), no influence on the isotherm pattern can be identified (Fig. 7a).

The location of the permeable fault, however, can be observed by locally disturbed isotherms directly below the salt rim syncline at the northern flank of the central salt pillow (solid black rectangle in Fig. 7a). A zoom into this fault-induced temperature anomaly reveals that the isotherms are sharply bent convex upward at the upper tip of the fault (Fig. 7b). This convex upward isotherm pattern continues upwards and diminishes toward the top of the overlying salt layer. By contrast, the isotherms are shaped convex downward at the lower tip of the fault. This thermal pattern continues downward throughout the underlying

Fig. 7 a Temperature distribution of the fault model 3 on the same vertical cross section as Fig. 5a. The location of the permeable fault cutting the central part of the cross section below the salt rim syncline is framed by the *black rectangle*. The locations where the two fault barriers dissect the profile are framed by a *dotted black rectangle*. **b** Zoom on the temperature distribution around the permeable fault as indicated by the *black rectangle* in **a**. Convex upward shaped isotherms at the faults upper tip and convex downward shaped isotherms at the lower tip form a thermal anomaly induced by the permeable fault. **c** Fluid velocity vectors (length non-scaled) and temperature distribution with reduced intensity in the background. The fluid flow in the subsalt sequence is influenced by the three faults dissecting this profile for which **d–e** display zooms into the fault areas for **d**, **f** the impermeable faults and for **e** the permeable fault

basement layer. In the central part of the fault (at its mid-depth), the temperatures are equal to the thermal field adjacent to the fault.

The overall isotherm pattern in the permeable fault displays a relatively uniform temperature distribution (144–148 °C) resulting in temperatures that are higher at the top and lower at the bottom of the fault compared to the no fault model (Fig. 5c). The fault-induced thermal anomaly indicates that the permeable fault locally impacts on the temperature field of the Rotliegend aquifer and also on that of the overlying salt and the underlying basement. Within these two layers, the heat from the fault is transferred not by fluids but by conduction due to the impermeable nature of salt and basement.

The appropriate flow field is shown in Fig. 7c as a combination plot of fluid velocity vectors and distribution of isotherms for the same vertical cross section (cf. Fig. 5a). Figure 7d, f shows zooms into the location of the

two fault barriers in the N and S parts of the cross section, whereas Fig. 7e illustrates a zoom into the permeable fault area in the central part (cf. Fig. 7b).

The velocity vectors expose an influence of the faults on the fluid circulation within the Rotliegend aquifer (Fig. 7c). Although the isotherm pattern is not affected by the fault barriers, the vectors indicate fluid deviation along these faults (Fig. 7d, f). Along both fault barriers downward flow occurs with decreased velocities ($\sim$1E$-$7 to 3.8E$-$10 m/day), but no fluid flow can be traced in their central parts. This observation indicates a fluid stagnation zone within the fault barriers in which no significant quantities of fluids can be transmitted due to the impermeable conditions and confirms that the heat is transmitted by conduction there.

By contrast, the fluid circulation and velocity are significantly influenced within and around the permeable fault (Fig. 7e). At mid-depth and at the lower tip, fluid vectors display fluid flow toward the fault from the surrounding

sediments. In the fault center, the vectors indicate upward oriented flow with highest velocities up to 0.03 m/day. At the upper tip, the fluid spreads out of the fault and moves laterally and downward along its flanks.

From surrounding sediments toward fault, the fluid advection is induced the by high permeability contrast between these two domains (Tables 1, 2) and causes thermal equilibration there. This equilibration leads to the observed relatively uniform temperature distribution ranging between 144 and 148 °C in the permeable fault (Fig. 7b). The upward moving fluid finally spreads out at the upper tip of the fault because it cannot enter the overlying impermeable Zechstein salt.

To track the thermal state and fluid movement along the entire permeable fault, the distribution of isotherms with flow vectors is shown along the entire fault plane in Fig. 8. The isotherms reveal alternating convex upward and downward shapes with corresponding hotter (140–148 °C) and colder (132–140 °C) domains. The flow vectors display a vigorous fluid circulation within the permeable fault. The colder domains roughly correspond to downward oriented flow whereas the hotter domains consort with upward oriented flow. At the upper tip, the vectors also indicate horizontal flow along the fault plane.

The higher fault permeability enables up and downward fluid flow with increased velocities as displayed by the vectors in the fault center in Fig. 7e. The differently oriented vectors reflect the convex up and downward shaped isotherm pattern which is characteristic for convective flow (cf. Fig. 5c, d). Within the fault, heated fluid becomes less dense due to thermal expansion. The buoyant fluid rises, cools and finally flows downward again due to its increased density. The observed horizontal flow at the upper faults tip is induced by the overlying Zechstein salt that acts as a sealing rock. As a consequence, the fluid spreads out of the faults top and distributes along both sides of the fault (cf. Fig. 7e).

Horizontal temperature distribution

Figure 9a, b shows the temperature distribution on a horizontal slice cutting the no fault model 2 and fault model 3 at a constant depth of −4,000 m. A temperature difference map between the two models is shown for −4,000 m depth (Fig. 9c). At this depth, the upper tips of the faults come close to the base of the Zechstein layer.

The temperature patterns for model 2 (Fig. 9a) and model 3 (Fig. 9b) correlate with the thickness of the Zechstein layer (Fig. 2a): in the SW model area, where the salt has thicknesses close to zero, the temperatures are significantly higher (up to 40 °C). On the contrary, in areas with increased salt thicknesses in the central and E parts of

the model, we find lower temperatures (range 112–120 °C) below the major NE and NW trending thick salt ridges.

By comparing the temperature distribution of the fault model 3 (Fig. 9b) with that of the no fault model 2 (Fig. 9a), it can be seen that the permeable NE–SW trending fault influences the temperature field: at the SW tip, isotherms trend toward the fault entry, indicating higher temperatures (∼142–144 °C) compared to the same area in model 2 (∼134–138 °C). In the central part of the fault, the isotherms display values between 142 and 146 °C decreasing toward the NE tip (132–140 °C), where the temperatures in the no fault model 2 range between 110 and 124 °C. The varying temperatures in different parts of the permeable fault reflect the alternating hotter and colder domains caused by the convective fluid circulation within the fault (cf. Fig. 8).

The corresponding temperature difference map between model 2 and 3 shows that the temperatures in the permeable NE–SW trending fault are up to 15 °C higher than in the no fault model 2 (Fig. 9c). The temperature differences are largest in the NE part of the fault. There, also the range of influence of the fault covers a maximum distance of ∼4.8 km. Though the overall temperature range is limited within the entire fault (132–148 °C), larger temperature differences occur below the major salt structures, where the surrounding thermal field is cooler (Fig. 9a). With increasing distance from the fault, the temperature differences gradually decrease indicating an equilibration with the matrix thermal field (cf. Fig. 7b, e).

The temperature distribution in −4,400 m depth is shown in Fig. 9d for the no fault model 2 and in Fig. 9e for the fault model 3. The horizontal slice mainly cuts the Lower Rotliegend Volcanics, representing the lowermost unit cut by the faults. Figure 9f depicts the temperature differences between the two models at the same depth. Compared to the temperature field in −4,000 m depth (Fig. 9a), the temperatures in model 2 are up to 15 °C higher at −4,400 m depth (Fig. 9d). Locally increased temperatures occur in the SE and E, where the salt thickness is close to zero, whereas locally reduced temperatures evolve in the W, below the thickest salt ridges. Comparing the predicted temperatures for the two models reveals that the temperatures in the fault are cooler than in the no fault model (Fig. 9d, e). Similar to −4,000 m depth (Fig. 9b), the temperatures range between 142 and 146 °C at the SW tip, between 140 and 144 °C in the central part and decrease toward the NE tip (134–140 °C).

The similar temperatures observed at both depths result from fluid advection from the surrounding sediments into the fault (cf. Fig. 7c, e).

In contrast to −4,000 m depth, the temperature difference map at −4,400 m (Fig. 9f) indicates temperatures that

Fig. 8 Temperature distribution along the entire permeable fault with fluid vectors (length non-scaled). Alternating hotter (140–148 °C) and colder domains (132–140 °C) with corresponding convex upward and downward shaped isotherms indicate convective heat transport and vigorous fluid flow within the permeable fault
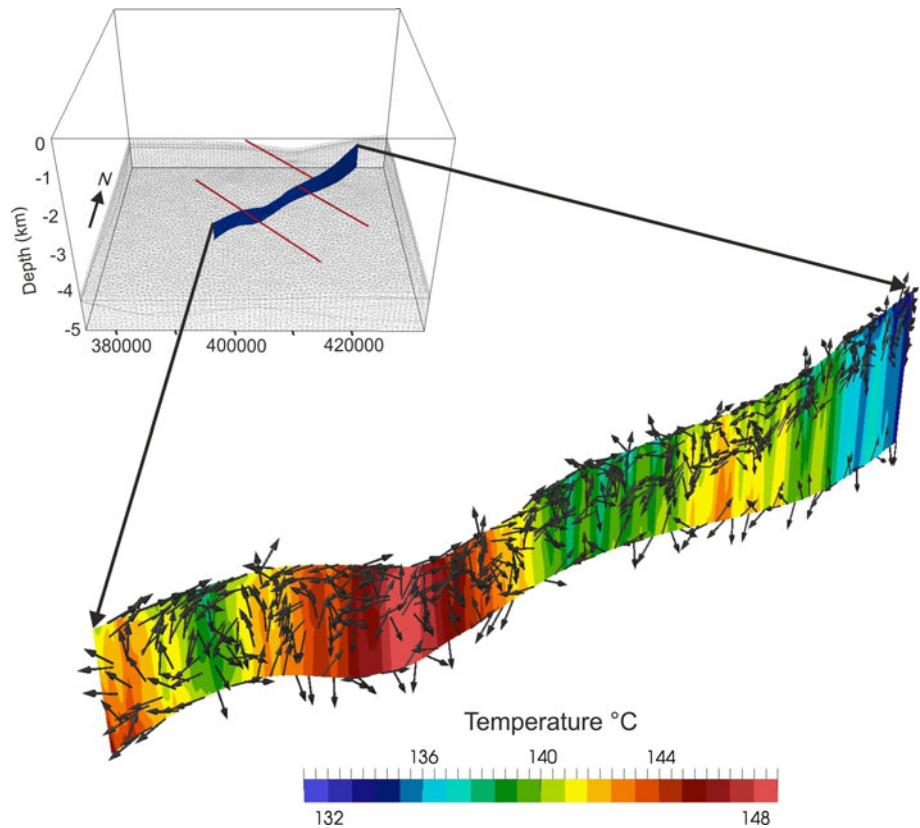
are up to 12 °C lower in the fault compared to the no fault model 2. The temperature differences are highest in the SW model area, where the temperatures are significantly higher in the matrix thermal field (cf. Fig. 9d).

Both temperature difference maps in −4,000 m and −4,400 m depth demonstrate that the fault barriers have no impact on the thermal field (cf. Fig. 7a)

Comparsion between modeled and measured temperatures

In all well locations (Fig. 6a–g), the modeled temperature curves of the fault model 3 are similar to the no fault model 2 generally fitting well with the observation data. Despite the fact that the locations of the wells Zehdenick 1/74 and GrSk 3/90 are close to the NW-SE trending fault barriers (Fig. 2c), no temperature variations between fault and no fault model are observed. This temperature trend confirms that the thermal field is not influenced by the fault barriers (Figs. 7a, 9c, f).

Pressure

The calculated pressure of both the fault and no fault model ranges between ∼40 MPa in −4,400 m and ∼44 MPa in −4,400 m which corresponds to the observed hydrostatic

pressure conditions in the Groß Schönebeck reservoir (Huenges et al. 2001).

In Fig. 10a and b, the pressure differences are depicted between the models 2 and 3 at −4,000 m and −4,400 m depth. In both figures, negative values indicate a lower pressure in the fault model whereas positive values correspond to a higher pressure in the fault model.

In −4,000 m depth, the pressure differences are in the range of −43 to −15 kPa. Pressure drops (∼−30 to 35 kPa) develop within the NW-SE trending fault barriers (Fig. 10a) and pressure offsets can be observed around them. Likewise, the pressure is reduced in the permeable fault, particularly at its tips (∼−30 to 43 kPa). This pressure drop correlates with the highest topographic elevation of the permeable fault plane in the NE and SW (cf. Fig. 8). Pressure offsets around the barriers are caused by the high permeability contrasts between faults and surrounding Rotliegend sediments (Tables 1, 2).

In −4,400 m depth, the pressure differences range from −7 to 60 kPa (Fig. 10b). Here, the pressure is higher in the faults (∼20–50 kPa) compared to the no fault model 2. Within the impermeable faults, the pressure differences are relatively uniform (∼40 kPa). In the conduit, the pressure increase is more pronounced in areas where the fault reaches greatest depths in the SW parts and in the NE (cf. Fig. 8). Similar to −4,000 m, pressure offsets develop
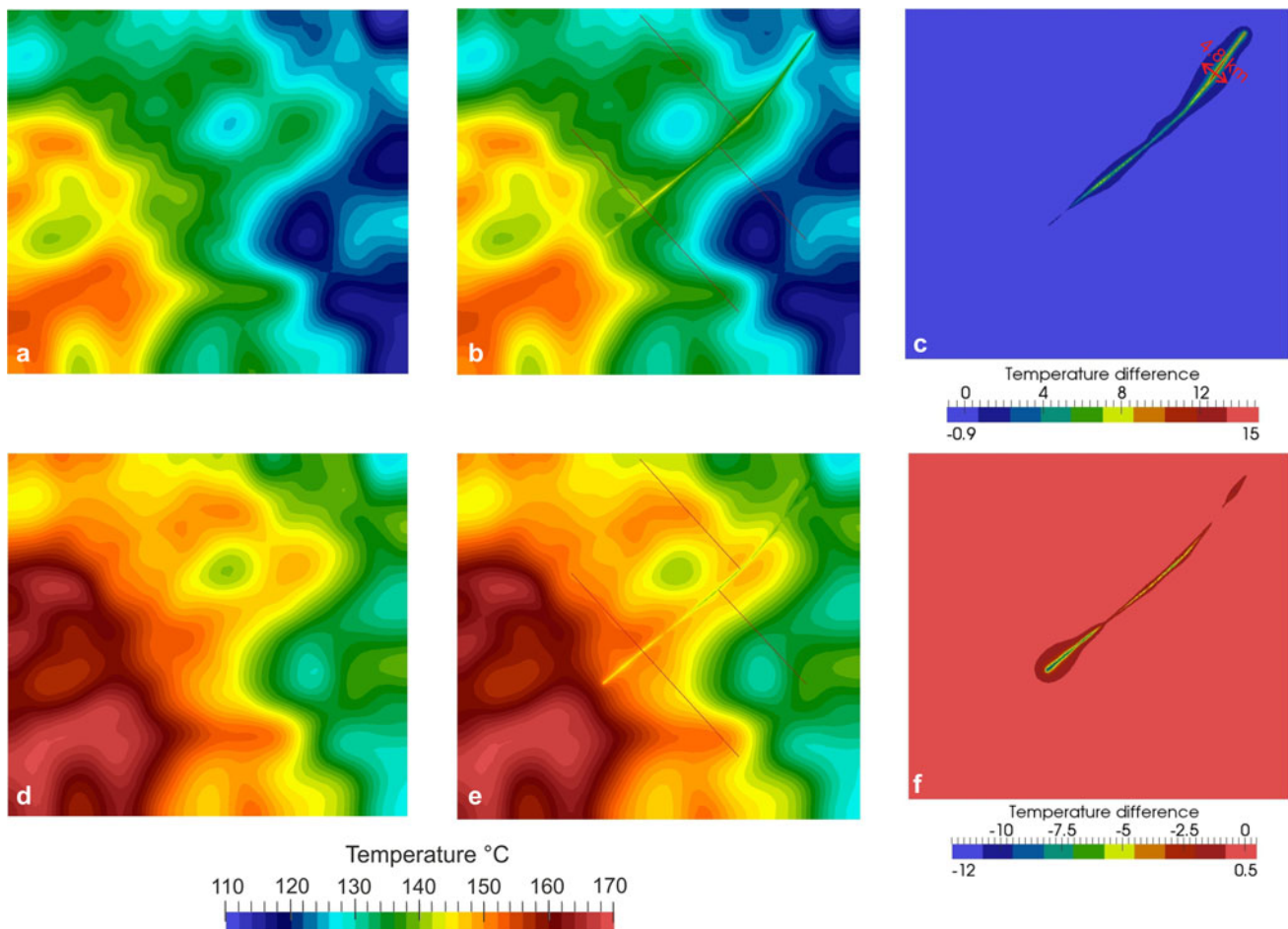
Fig. 9 Temperature distribution on a horizontal slice in −4,000 m depth cutting **a** the no fault model 2 and **b** the fault model 3 whereas **c** displays the corresponding temperature difference map in which the no fault model 2 is subtracted from fault model 3. Positive values indicate higher temperatures in the fault model and vice versa. The temperature differences are up to 15 °C higher in the NE–SW trending permeable fault than in the no fault model 2. Note the area influenced by the latter encompasses ∼4.8 km at the NE tip of the fault (*red arrow*). Temperature distribution on a horizontal slice in −4,400 m depth cutting **d** the no fault model 2 and **e** the fault model 3. **f** The temperature difference map in which the no fault model 2 is subtracted from fault model 3. Positive values indicate higher temperatures in the fault model and vice versa. In contrast to −4,000 depth, the temperatures in the permeable fault are up to −12 °C cooler than in the no fault model 2

around the impermeable faults due to the high permeability contrasts between faults and surrounding sediments.

Discussion and conclusions

The 3-D conductive and coupled fluid and heat transport simulations and the integration of faults into the system revealed several specific controlling factors for the thermal field.

Conduction

Assuming thermal conduction as the only heat transport mechanism reproduces the thermal observations in those parts of the model where layers are impermeable. Those layers comprise the Tertiary Rupelian, the Triassic Muschelkalk and the Permian Zechstein and the Basement. There, the contrasts in thermal conductivities decisively shape the temperature distribution. The most obvious effect of this type is the influence of the thermally highly conductive Zechstein salt. This strong impact of the Permian Zechstein salt on the deep thermal field is consistent with results from previous modeling studies in the North German Basin (Bayer et al. 1997; Cacace et al. 2010; Kaiser et al. 2011; Noack et al. 2010; Scheck 1997; Sippel et al. 2013; Magri 2005). The salt leads to a focused transfer of heat, amplified in salt structures like diapirs and pillows where the characteristic di-pole shaped thermal anomalies develop.

In our conductive model, the temperatures are too hot compared to the temperature observation from the different
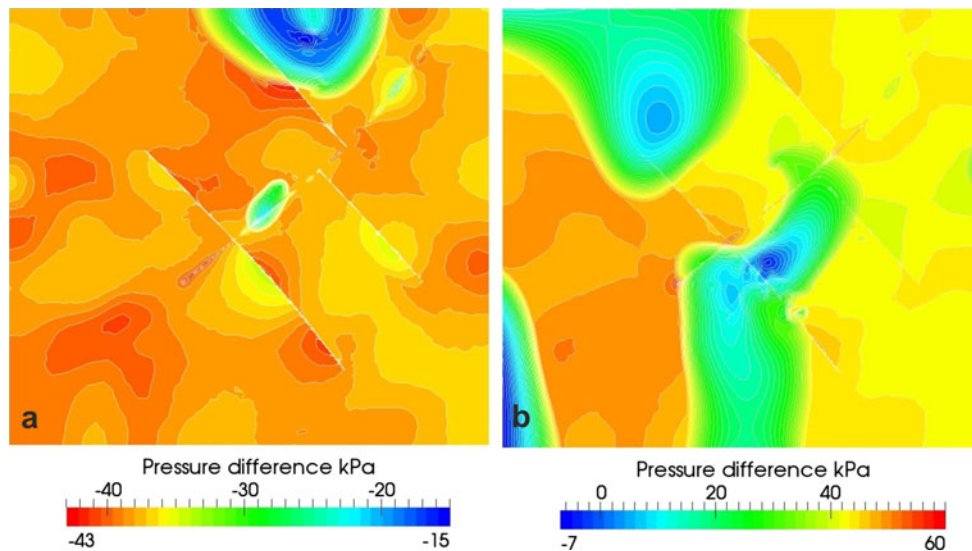
Fig. 10 Pressure differences between no fault model 2 and fault model 3 **a** at −4,000 m depth and **b** at −4,400 m depth. Positive values indicate a lower pressure in the fault model whereas negative values correspond to a higher pressure in the fault model. Pressure offsets are visible and most prominent around the NW–SE oriented impermeable faults

wells, apart from well measurements obtained from the Zechstein salt. For the remaining parts of the model, relatively large deviations occur between modeled and observed temperatures, suggesting that additional heat transfer processes are active that modify the temperature distribution.

Advection

Accordingly, fluid flow considered in addition to heat transport within a coupled simulation reproduces observed temperatures better in those domains where permeable layers are present. In comparison to the conductive model, suppressed isotherms show that the fluid flow has an overall cooling effect induced by the upper thermal boundary condition. This cooling effect reaches greater depths in areas where the Rupelian is missing because cold water can flow unhampered into the Mesozoic aquifer. Additional local pathways for the cold water inflow are provided by Quaternary channels, hydraulically connecting the Quaternary with the Mesozoic aquifer. The influence of advective cooling through topography-driven fluid flow on the temperature field has been demonstrated previously by 2-D flow and heat simulations along the northern Rheingraben (Lampe and Person 2002). Furthermore, simulation results of 2-D thermohaline models of the North German Basin indicate that the inflow of freshwater reaches the Pre-Rupelian aquifer even in areas where the Rupelian is thin and that this inflow is favored by Quaternary channels (Magri et al. 2008). In summary, our results suggest that cooling due to topography-driven fluid flow may reach down to depths of maximum −1,800 m if the Rupelian layer provides adequate windows.

Convection

In addition to advective cooling, the overall temperature distribution of the coupled fluid and heat transport model is influenced by convective heat transfer closely linked to the distribution of permeable aquifer systems and impermeable aquicludes.

In the suprasalt sequence, convection cells develop in the Mesozoic aquifer, where the latter is sufficiently thick and permeable. Both thickness (i.e. water column) and permeability of the sediments are the most critical factors for the Rayleigh number which expresses the conditions required for thermal convection (Bjørlykke 2010). The underlying thin and low-permeable Muschelkalk aquiclude, however, decouples the flow system into the Mesozoic aquifer above and the Buntsandstein aquifer below. Although thermally induced instabilities can be observed within the Buntsandstein aquifer, its thickness is obviously insufficient for the development of convection cells.

In conclusion, the supra-salt unit is predominantly influenced by advective heat transport in the Cenozoic and shallow part of the Mesozoic aquifer (up to maximum −1,800 m depth) counteracted by convective heat transport within the latter.

In contrast, the temperature distribution of the subsalt system appears to be mainly influenced by conduction and by a thermal feedback with the overlying layers. Although there are indications for weak fluid circulation in the

permeable sediments of the Rotliegend aquifer, fluid velocities ($\sim$1E−08 to 1E−10 m/day) are too slow to cause significant temperature anomalies. This observation leads to the conclusion that conduction outweighs the heat transfer via fluids in the Rotliegend aquifer.

However, the generally good fit between the modeled temperatures of the coupled fluid and heat transport simulation and the observed values suggests that fluid flow processes play an important role in the heat transfer mechanisms controlling the overall thermal field of the Groß Schönebeck area. This finding disagrees with earlier results from a conductive thermal model of the Groß Schöeneck test site (Ollinger et al. 2010) and of the Brandenburg area (Noack et al. 2010) stating that the entire thermal regime in the region is dominated by conduction. However, our results confirm that the moderate permeability of the Rotliegend aquifer, combined with a comparably small thickness, prevents that convection could alter the diffusive thermal regime (cf. Ollinger et al. 2010). We agree with Noack et al. (2012) in that moving fluids in restricted areas may influence the deep thermal field of the Brandenburg area. Furthermore, coupled simulations of fluid and heat as well as mass transport for the E part of the North German Basin confirm that thermally induced convection at the basin scale is feasible though locally restricted (Kaiser et al. 2011; Magri 2005). In accordance with these results, we suggest that induced convective circulation in the shallower aquifers decisively shapes the thermal field in the Groß Schöeneck area, whereas a convective influence in the deep Rotliegend aquifer can be neglected.

Comparison to other models

The comparison of the modeling results with temperature estimations by Agemar et al. (2012) shows a generally good fit with the coupled model 2 at −4,000 m and −4,400 m depth (Fig. 9a, d). A similar regional temperature trend can be observed in both maps. At −4,000 m depth, highest temperatures (150–155 °C) characterize the SW model area, while temperatures vary between 145 and 150 °C in the W in both cases. In the northern part, minor differences are observed with temperatures ranging between $\sim$138 and 140 °C in the coupled model 2, compared to temperatures of $\sim$140–145 °C by Agemar et al. (2012). In the central part (around the location of the well GrSk 3/90), the temperatures are similar in both maps (135–140°). By following the regional temperature trend (Fig. 9a, d), temperatures gradually decrease toward the S and the E parts in the two cases. In the SE and E model area, however, temperatures of the coupled model 2 are generally $\sim$10–15 °C colder than the values estimated by Agemar et al. (2012). The cooler temperatures in the SE/E

model domain are induced by the location below the major salt ridges. Temperatures are additionally decreased by a thermal feedback from net cooling in the shallow Mesozoic aquifer due to unhampered cold water inflow through the "Rupelian windows" (areas where the clay has been eroded or not deposited). This net cooling may overestimate the impact of cold water advection due to the chosen upper boundary conditions (see "Model limitations").

Model limitations

Despite the generally nice fit of the fluid and heat transport simulation with well measurements and the temperature estimations by Agemar et al. (2012), some deviations occur between modeled and predicted temperatures.

These deviations could be related to several reasons such as: (1) the choice of physical properties assigned for the geological units; (2) the structural limitations of the model; and (3) the choice of boundary conditions.

1. Since the hydraulic properties, especially the permeability, are a crucial factor in influencing the fluid and thermal system, the choice of values is important. The hydraulic properties used for the simulations are based on spatially available data (Čermák et al. 1982) which have been averaged to basin scale (i.e. km) (Magri 2005; Magri et al. 2008). Using the same properties, a variety of modeling studies established in the E part of the NGB (Cacace et al. 2010; Kaiser et al. 2011; Kaiser et al. 2013; Noack et al. 2013; Pommer 2012; Przybycin 2011) confirm that these values represent effective properties when investigating the controlling physical processes at basin scale (i.e. process-oriented modeling) and furthermore benefit from being comparable to each other. Moreover, they proved that these values, comprising thermal and hydraulic properties, match observed temperatures from wells (Noack et al. 2012, 2013). However, the assumption of a uniform distribution of physical properties does not reflect the heterogeneity of the respective layers (Noack et al. 2012). Therefore, a certain degree of uncertainty remains due to the spatial variability of hydraulic properties (Magri 2005; Magri et al. 2008) and could easily vary an order of magnitude. For this reason, additional simulations are conducted for both the supra- and the subsalt sequence to assess the sensitivity of the model with respect to the physical parameters.

   Since in the shallow model domain, the Rupelian clay plays an important role in affecting the fluid flow, the permeability of the Rupelian is decreased to $k = 1\text{E}{-}18$ m^2, representing an appropriate permeability value for plastic clay in an additional simulation. The

simulation results generally show higher temperatures, especially in areas where the Rupelian clay is present with highest thicknesses (in the W). The temperature increase is strongest in the shallow Cenozoic and Mesozoic layers (mean range 0–30 °C). In the deeper subsalt sediments, the thermal pattern converges, but still slightly higher temperatures (∼0–15 °C) are present, confirming the thermal feedback of the suprasalt on the subsalt model domain. The comparison with the measured temperatures shows a better fit than for the coupled model 2, assuming a higher permeability for the Rupelian. A generally good fit is observed for the wells Grüneberg 2/74 (Table 4) and GrSk 3/90 (Table 5); in the other wells, the temperatures are similar or slightly increased compared to the coupled model 2 (Tables 4, 5).

Sensitivity analyses for the permeability values in the Cenozoic and Mesozoic layers have been also run by Noack et al. (2013) by 3-D coupled fluid and heat transport simulations for the Brandenburg area. Major outcomes from this study were that decreased permeabilities for the Pre-Rupelian clay formations lead to rising temperature values close to the results from conductive modeling and that advective cooling is strongly reduced if a decreased permeability by one order of magnitude is considered for the Quaternary and Tertiary layers.

Overall, the dependence of the permeability on the modeling results and its uncertainty calls for sensitivity studies for this parameter and ongoing work.

For the subsalt sequence, we tested other sets of thermal and hydraulic properties for the conductive and coupled models. Focusing on the deviations between modeled and predicted temperatures observed in the subsalt sequence (Fig. 6a), an end-member set, listed in Table 1 (values in brackets) has been chosen. The reason for this choice is that the properties are better resolved for the subsalt layers including the Rotliegend (reservoir) aquifer compared to the original set of properties (Table 1, values outside brackets). The end-member set contains hydraulic and thermal properties of the Rotliegend aquifer reservoir rocks measured under in situ conditions (Blöcher et al. 2010). Furthermore, higher values of radiogenic heat production rates for the Cenozoic to Upper Permian Zechstein and a higher thermal conductivity for the Permian Zechstein salt are used (Norden and Förster 2006; Norden et al. 2008). The temperature trends of these simulations are similar to the model results with the original set of properties (Table 1). Temperature differences (in the range 0–5 °C) occur only within the Zechstein salt and its proximity. The temperatures of the model with the end-member property set are higher on top and lower at the bottom of the salt, by comparison. The maximum differences (up to 5 °C) are observed in well locations where the salt thickness is largest (Fig. 6c–e) whereas in areas with lower salt thickness the differences are very small (0–1 °C) (Fig. 6a, b, f, g). The enhanced impact of the salt is caused by its higher thermal conductivity compared to the original set of properties (Table 1). From the results of this sensitivity study, we can conclude that the deviations between modeled and predicted temperatures are not primarily linked to the property assignment.

2. Those components of the misfit that could be related to structural limitations of the model and/or, as already addressed in the previous section, to lithological heterogeneities not considered in the property assignment of the individual geological layers (Fig. 6a) are more difficult to assess. Quantifying effects of this type would require a more detailed consideration of structural input data and physical properties.

3. The misfit in shallower depth (Fig. 6b) could be related to the chosen upper boundary conditions triggering a constant inflow of cold water during the simulation. It remains to investigate to which degree this thermal condition influences the overall temperature distribution and thermal evolution within the coupled simulations. This should consider also realistic information on recharge conditions and the coupling with surface water transport.

A further influencing factor which might enlarge the offset of the observed temperatures and especially the conductive thermal model is the spatially varying heat flux used as the lower boundary condition. The basal heat flux is extracted from a conductive thermal model of Brandenburg which is extended down to the Lithosphere–Asthenosphere Boundary (LAB) and takes into account a differentiated crust (Noack et al. 2012). This model generally fits well to observed temperature data from wells. Yet a small degree of uncertainty may persist due to a partly overestimation of the temperatures. However, the results should be considered as a good approximation given the fact that the model is consistent with temperature, deep seismic and gravity observations. Therefore, it represents a profound base for defining the lower thermal boundary conditions of the smaller-scale Groß Schönebeck model.

Altogether, the relatively small size of the model combined with the laterally closed boundaries for fluid and heat transport may in addition favor a stronger impact of the adopted boundary conditions compared to larger scaled models. Future studies should consider the assignment of lateral boundary conditions extracted from larger scaled fluid and heat transport models.
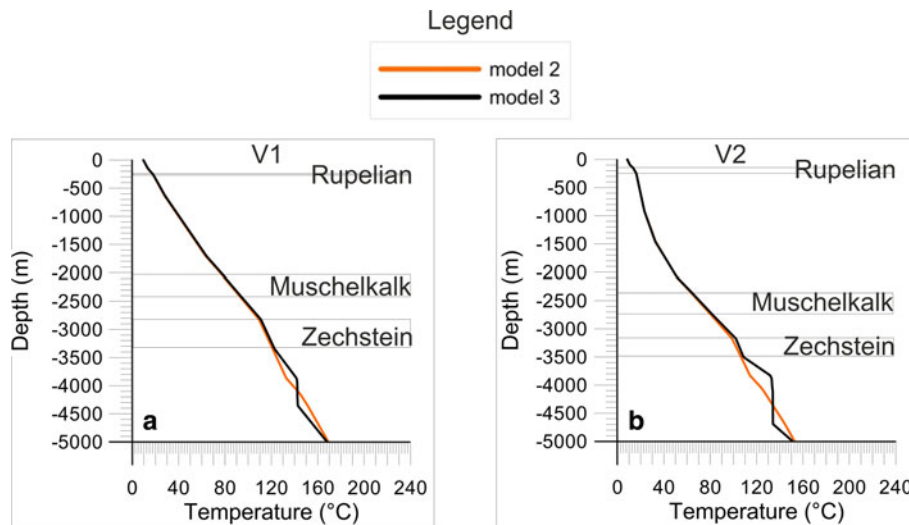
Fault model

The results of the model in which subsalt major faults are included reveal a local and strong influence of the permeable NE-SW trending fault. The temperature distribution and the velocity vectors indicate convective flow in the fault (~0.001 m/day). Lateral fluid advection from surrounding sediments into the fault is induced by the high fault permeability. In the fault, the convective heat transport leads to an equilibration of the temperatures. This results in the observed higher temperatures at the top (−4,000 m depth) and lower temperatures at the base (−4,400 m depth) compared to the no fault model. Above and below the fault, heat is transferred by conduction due to the impermeability of the underlying Basement and the overlying Zechstein salt. Additionally, the salt prevents the fluid to move upwards which causes lateral flow at the upper tip of the fault and downward flow along the fault's flanks.

Convective flow in permeable faults has also been proposed earlier. Yang (2006) simulated fluid flow and heat transport based on a highly idealized 3-D model of the McArthur Basin (Northern Australia) including two subvertical permeable faults. The results demonstrated that significant fluid circulation takes place mainly within the more permeable faults rather than in the host rocks and that both upwelling and downwelling flow develop within the two faults at different longitudinal distances giving rise to temperature variation along the fault strike direction. Other coupled simulations of fluid flow, heat transfer and reactive mass transport with an idealized 3-D section of a vertical fault system showed that finger-like convection can arise in the fault zone (Alt-Epping and Zhao 2010). Similar to our findings, the results indicated vigorous fluid flow throughout the fault plane that promotes thermal homogenization there.

Additional simulations were carried out to consider the effects of flower permeability values of the fault on the surrounding groundwater and thermal field (not shown). Convective flow has been observed in the conductive fault even for a lower permeability value in the fault. In general, few quantitative data are available to provide geologically plausible permeability values for faults and fault-like features incorporated in numerical simulations (Evans et al. 1997). Because technology does not allow the acquisition of detailed property distributions from within active faults (Fairley 2009), most information on fault property distributions in the published literature is derived from studies of exhumed paleofaults (e.g. Antonellini and Aydin 1994; Caine et al. 1996; Rawling et al. 2001) or borehole testing in active faults (e.g. Barton et al. 1995). Laboratory-determined permeabilities for natural fault core materials show a range of variation of approximately 10 orders of magnitude (1E−12 to 1E−22 m^2 from Smith et al. 1990) (Caine et al. 1996). Evans et al. (1997) inferred that fault core materials may be characterized by the lower end of the permeability range (about 1E−17 to 1E−18 m^2, whereas more heterogeneous damaged zone materials may be characterized by the wider range of higher permeabilities (1E−16 to 1E−11 m^2). Most of the numerical studies of different geological settings or based on synthetic models use values in the range of 1E−11 to 1E−14 m^2 for conductive faults (e.g. Alt-Epping and Zhao 2010; Bächler et al. 2003; Bense et al. 2008; Cacace et al. 2013; Clauser and Villinger 1990; Fairley 2009; Geiger et al. 2004; Lampe and Person 2002; López and Smith 1995; Magri et al. 2010; Simms and Garven 2004; Yang 2006), whereby the mean value is around $k = 1E−13$ m^2 and a sufficient permeability contrast between the fault- and the host rock domain is even assured. For this study, mean permeabilities around 1E−13 m^2 have been initially used for the conductive fault, due to a lack of information on fault composition and property data. However, no effect was observed on the hydrothermal field, which is ascribed to the (too) low permeability contrast between fault and surrounding sediments ($k = 1E−14$ m^2, Table 1). To ensure a sufficiently high permeability contrast between fault and surrounding sediments, a higher permeability value was set for the conduit ($k = 1E−9$ m^2, Table 2), characterizing the higher end of the permeability range. Furthermore, sensitivity tests have been conducted with lower fault permeabilities. The assumption of a fault permeability in between moderate (1E−13 m^2) and high permeability (1E−09 m^2) of $k = 1E−11$ m^2 shows a more pronounced convective thermal pattern in the fault within a slightly broader temperature range (118–154 °C) with respect to the more permeable fault (131–149 °C). As a result of the lower permeability, fluid velocities decrease up to two orders of magnitudes compared to the highly permeable fault. Despite these differences, the first order mechanisms that control the fluid and heat transport in the fault remain the same as well as the range of influence on the thermal field.

Although our results indicate a significant impact of the permeable fault on the thermal field, the fault model temperature curves are similar to the no fault model 2 in all well locations and both reproduce the observation data similarly well. This is related to the fact that none of the wells is located adjacent to the NE–SW oriented permeable fault. To quantitatively assess the thermal impact of the permeable fault, we plotted the calculated temperatures for the no fault and fault model for two virtual wells (Fig. 11a, b) along the fault (locations in Fig. 6). The plots reveal temperature difference of up to 10 °C below the Zechstein layer and confirm a significant impact of the permeable fault on the thermal field along the fault. By contrast, the

Fig. 11 Calculated temperatures-depth gradients for two virtual wells in the **a** SW and **b** NE parts of the NE-SW oriented permeable fault. Their locations are displayed in Fig. 6 in V1 and V2, respectively. The modeled temperatures for the no fault model 2 are represented by *solid orange lines* and for the fault model 3 by *black solid lines*. The depth position of the Rupelian, the Muschelkalk and the Zechstein layers is outlined by *gray lines* in the background in both figures. Below the Zechstein layer significant temperature differences demonstrate the local impact of the permeable fault on the thermal field

temperature field is not influenced by the NW–SE trending fault barriers. No significant quantities of fluids can be transmitted due to the impermeable conditions and thus conduction is the predominant heat transport mechanism like in the surrounding sedimentary Rotliegend. Accordingly, no thermal signal is imprinted by the low permeable faults because the thermal properties of the barriers do not differ from sedimentary matrix.

Nevertheless, the fault barriers induce minor deviation of the matrix flow, which is not effective enough to cause temperature variations in the surroundings of the faults. Increasing the spatial extent of the barriers may enhance their impact on fluid circulation and thermal field. However, the fact that the barriers influence the pressure field is obviously independent from their spatial extent. This finding is in agreement with Haneberg (1995) who stated that the effectiveness of a low-transmissivity fault as a pressure seal is independent of the fault thickness in absence of fault zone and discharge.

Conclusions

Our results suggest that different heat transport processes closely linked to the distribution of aquifers and aquicludes mainly control the deep thermal field in the study area. The better fit of the coupled fluid and heat transport model with observed temperatures demonstrates the importance of 3-D geologically constrained simulations for assessing the temperature distribution in the subsurface.

Beyond, our results indicate that the consideration of faults, which are more permeable than the host aquifer, is necessary for geothermal exploration because they can exert a strong control on the thermal field and on fluid circulation on a local scale.

The final temperature distribution is the superposed result of all these processes. Conductive, advective and convective heat transport control the temperature field in the suprasalt aquifers providing a thermal feedback superposed on the conductive regime in the subsalt aquifer. The matrix thermal field influences the temperature distribution in the fault, further modified by convective circulation within the latter. The fault itself generates in turn a thermal feedback for the bounding impermeable layers by transferring its locally modified heat to its conductive neighbors.

Assessing the complexity of the different interacting processes represents an important step to understand the specific controlling factors for a complex hydrogeological setting with natural fault zones for an area used for geothermal exploitation.

Appendix

The following governing equations are solved by the numerical simulator FEFLOW® (Diersch 2002):

$$\frac{\partial(\varepsilon\rho^f)}{\partial t} + \nabla \cdot (\rho^f \mathbf{q}^f) = \rho^f Q_\rho \tag{1}$$

Equation (1) represents the mass conservation of the fluid with variable mass density of the fluid (ρ^f), porosity (ε), specific discharge (Darcy's velocity $(\mathbf{q}^f)$) and the sink/source mass term (Q_ρ).\

$$\mathbf{q}^f = -\mathbf{K}\left(\nabla h + \frac{\rho^f - \rho_0^f}{\rho_0^f}\frac{\mathbf{g}}{|g|}\right) \tag{2}$$

Equation (2) expresses the generalized Darcy's law with the hydraulic conductivity tensor $(\mathbf{K})$ of the porous media given by $\mathbf{K} = \frac{\rho_0^f g}{\mu^f}\mathbf{k}$, with the permeability tensor $(\mathbf{k})$, the dynamic fluid viscosity μ^f, and the gravity acceleration (g).

$$(\rho c)_{fs}\frac{\partial T}{\partial t} + \rho^f c^f \nabla \cdot (\mathbf{q}^f T) - \nabla \cdot (\lambda \nabla T) = Q_T \tag{3}$$

The heat transport equation (3) results under the assumption of thermal equilibrium between the fluid and the porous medium and if density gradients are neglected in the Darcy law (Eq. 2), with $(\rho c)_{fs}$ being the specific heat capacity of the fluid (f) plus solid (s) phase system, defined as

$$(\rho c)_{fs} = \varepsilon\rho^f c^f + (1-\varepsilon)\rho^s c^s \tag{4}$$

Q_T is the heat source function. λ represents the equivalent thermal conductivity tensor of the porous medium and the fluid which takes both (Fourier's) and thermodispersive (mixing) effects into account. The equivalent thermal conductivity may be split into two components:

$$\lambda = \lambda_{\text{DISP}} + \lambda_{\text{COND}} \tag{5}$$

where the first term on the right hand side of Equation (5) is the thermodispersive term with the longitudinal (α_L) and transversal (α_T) dispersion lengths:

$$\lambda_{\text{DISP}} = \rho^f c^f \left[\alpha_T \sqrt{(q_i^f q_i^f)} + (\alpha_L - \alpha_T)\frac{q_i^f q_i^f}{\sqrt{(q_i^f q_i^f)}}\right] \tag{6}$$

and the second term on the left hand side is the conductive term with the thermal conductivity of the fluid (λ^f) and solid phase (λ^s) and the unit matrix $(\mathbf{I})$:

$$\lambda_{\text{COND}} = \varepsilon\lambda^f + (1-\varepsilon)\lambda^s \tag{7}$$

The balance equations (2) and (3) are coupled by the fluid density compliant with an equation of state after Magri (2005); Blöcher et al. (2010).

References

Agemar T, Schellschmidt R, Schulz R (2012) Subsurface temperature distribution in Germany. Geothermics 44:65–77

Alt-Epping P, Zhao C (2010) Reactive mass transport modelling of a three-dimensional vertical fault zone with a finger-like convective flow regime. J Geochem Explor 106:8–23

Amante C, Eakins BW (2009) ETOPO1 1 Arc-minute global relief model: procedures, data sources and analysis. NOAA Technical Memorandum NESDIS NGDC-24

Antonellini M, Aydin A (1994) Effect of faulting on fluid flow in porous sandstones: petrophysical properties. Am Assoc Petrol Geol Bull 78:355–377

Bächler D, Kohl T, Rybach L (2003) Impact of graben-parallel faults on hydrothermal convection—Rhine Graben case study. Phys Chem Earth 28:431–441

Balling N, Kristiansen JI, Breiner N, Poulsen KD, Rasmussen R, Saxov S (1981) Geothermal measurements and subsurface temperature modelling in Denmark. Techn. Ber. GeoSkrifter, No. 16, Department of Geology, Aarhus University

Barton CA, Zoback MD, Moos D (1995) Fluid flow along potentially active faults in crystalline rock. Geology 23(8):683–686

Bayer U, Scheck M, Koehler M (1997) Modeling of the 3-D thermal field in the northeast German Basin. Geolog Rundsch 86:241–251

Bear J (1991) Modeling transport phenomena in porous media. Convective Heat and Mass Transfer in Porous Media, pp 7–69

Bense VF, Person MA, Chaudhary K, You Y, Cremer N, Simon S (2008). Thermal anomalies indicate preferential flow along faults in unconsolidated sedimentary aquifers. Geophys Res Lett 35(L24406). doi:10.1029/2008GL036017

Bjørlykke K (2010) Subsurface water and fluid flow in sedimentary basins. Petroleum geoscience: from sedimentary environments to rock physics. Springer, Heidelberg, pp 259–279. doi:10.1007/978-3-642-02332-3_10

Blöcher MG, Zimmermann G, Moeck I, Brandt W, Hassanzadegan A, Magri F (2010) 3-D numerical modeling of hydrothermal processes during the lifetime of a deep geothermal reservoir. Geofluids 10(3):406–421

Bundschuh J, Arriaga M (2010) Introduction to the numerical modeling of groundwater and geothermal systems. Fundamentals of mass, energy and solute transport in poroelastic rocks. Taylor & Francis, Boca Raton

BURVAL Working Group (2009) Buried Quaternary valleys—a geophysical approach. Zeitschrift der Deutschen Gesellschaft für Geowissenschaften 160(3):237–247

Cacace M, Kaiser BO, Lewerenz B, Scheck-Wenderoth M (2010) Geothermal energy: what we can learn from regional numerical models. Chem Erde 70(S3):33–46

Cacace M, Blöcher G, Watanabe N, Moeck I, Börsing N, Scheck-Wenderoth M, Kolditz O, Huenges E (2013) Modelling of fractured carbonate reservoirs—outline of a novel technique via a case study from the Molasse Basin, southern Bavaria, Germany. Environ Earth Sci. doi:10.1007/s12665-013-2402-3

Caine JS, Evans PE, Forster CB (1996) Fault zone architecture and permeability structure. Geology 24(11):1025–1028

Čermák V, Huckenholz H-G, Rybach L, Schmid R, Schopper J R, Schuch M, Stöffler D, Wohlenberg J (1982) Physical properties of rocks, vol 1, Subvolume a. In: Angenheister G (ed) Landolt-Börnstein, New Series, V/1a: Geophysics and Space Research. Springer, Berlin, pp 1–373

Clauser C, Villinger H (1990) Analysis of conductive and convective heat transfer in a sedimentary basin, demonstrated for the Rheingraben. Geophys J Int 100(3):393–414

Diersch H-JG (2002) FEFLOW Finite-element subsurface flow and transport simulation system. User's Manual/Reference Manual/White Papers, Release 5.0. WASY GmbH, Berlin

Evans JP, Forster CB, Goddard JV (1997) Permeability of fault-related rocks, and implications for hydraulic structure of fault zones. J Struct Geol 19(11):1393–1404

Fairley JP (2009) Modeling fluid flow in a heterogeneous, fault-controlled hydrothermal system. Geofluids 2009(9):153–166

Förster A (2001) Analysis of borehole temperature data in the Northeast German Basin: continuous logs versus bottom-hole temperatures. Pet Geosci 7:241–254

Geiger S, Roberts S, Matthai K, Zoppou C, Burri A (2004) Combining finite element and finite volume methods for efficient multiphase flow simulations in highly heterogeneous and structurally complex geologic media. Geofluids 4:284–299

Gudmundsson A, Fjeldskaar I, Brenner SL (2002) Propagation pathways and fluid transport in jointed and layered rocks in geothermal fields. J Volcanol Geotherm Res 116:257–278

Haneberg WC (1995) Steady state groundwater flow across idealized faults. Water Resour Res 31(7):1815–1820

Holl H-G, Moeck I, Schandelmeier H (2005) Characterisation of the tectono-sedimentary evolution of a geothermal reservoir—implications of exploitation (Southern Permian Basin, NE Germany). In: Proceedings of world geothermal congress 2005, Antalya, Turkey

Hudec MR, Jackson MPA (2007) Terra firma: understanding salt tectonics. Earth Sci Rev 82:1–28

Huenges E (ed) (2011) Geothermal energy systems: exploration, development, and utilization. Wiley-VCH, New York, pp 1–463

Huenges E, Poser M, Schrötter J (2001) Formationsdruck in der Bohrung Groß Schönebeck—Ableitung aus Pegelmonitoring nach Abschluss des Primärtestes. STR02/14, Geothermie Report 02-1

Huenges E, Hurter S, Saadat A, Köhler S, Trautwein U (2002) The in-situ geothermal laboratory Groß Schönebeck—learning to use low permeability aquifers for geothermal power. In: Proceedings of twenty-seventh workshop on geothermal reservoir engineering Stanford University, Stanford, California, January 28–30, 2002

Huenges E, Trautwein U, Legarth B, Zimmermann G (2006) Fluid Pressure variation in a sedimentary geothermal reservoir in the North German Basin: case Study Groß Schönebeck. Pure Appl Geophys 163:2141–2152

Ito T, Zoback MD (2000) Fracture permeability and in situ stress to 7 km depth in the KTB scientific drillhole. Geophys Res Lett 27:1045–1048

Kaiser BO, Cacace M, Scheck-Wenderoth M, Lewerenz B (2011) Characterization of main heat transport processes in the Northeast German Basin: constraints from 3-D numerical models. Geochem Geophys Geosyst 12:Q07011. doi:07010.01029/02011GC003535

Kaiser BO, Cacace M, Scheck-Wenderoth M (2013) 3D coupled fluid and heat transport simulations of the Northeast German Basin and their sensitivity to the spatial discretization: different sensitivities for different mechanisms of heat transport. Environ Earth Sci. doi:10.1007/s12665-013-2249-7

Katzung G (ed) after Kaiser et al (1984) Geothermie-Atlas der Deutschen Demokratischen Republik, Zentrales Geologisches Institut (ZGI)

Lampe C, Person M (2002) Advective cooling within sedimentary rift basins—application to the Upper Rhinegraben (Germany). Mar Petrol Geol 19:361–375

López DL, Smith L (1995) Fluid flow in fault zones: analysis of the interplay of convective circulation and topographically driven groundwater flow. Water Resour Res 31(6):1489–1503

Magri F (2005) Mechanismus und Fluiddynamik der Salzwasserzirkulation im Norddeutschen Becken: Ergebnisse thermohaliner numerischer Simulationen (Dissertation Thesis, Freie Universität Berlin). Scientific Technical Report STR05/12, GeoForschungs-Zentrum Potsdam, pp 1–131

Magri F, Bayer U, Tesmer M, Möller P, Pekdeger A (2008) Salinization problems in the NEGB: results from thermohaline simulations. Int J Earth Sci (Geologische Rundschau) 97:1075–1085

Magri F, Akar T, Gemici U, Pekdeker A (2010) Deep geothermal groundwater flow in the Seferihisar-Balçova area, Turkey: results from transient numerical simulations of coupled fluid flow and heat transport processes. Geofluids 10:388–405

Moeck I, Holl H-G, Schandelmeier H (2005) 3D Lithofacies model building of the rotliegend sediments of the NE German Basin. In: AAPG international conference and exhibition (Paris France 2005), CD-ROM, paper #98619

Moeck I, Schandelmeier H, Holl H-G (2009) The stress regime in a Rotliegend reservoir of the Northeast German Basin. Int J Earth Sci 98:1643–1654

Nield DA, Bejan A (eds) (2006) Convection in porous media. Springer, New York, pp 1–640

Noack V, Cherubini Y, Scheck-Wenderoth M, Lewerenz B, Höding T, Simon A, Moeck I (2010) Assessment of the present-day thermal field (NE German Basin)—inferences from 3D modelling. Chem Erde 70(S3):47–62

Noack V, Scheck-Wenderoth M, Cacace M (2012) Sensitivity of 3D thermal models to the choice of boundary conditions and thermal properties—a case study for the area of Brandenburg (NE German Basin). Environ Earth Sci. doi:10.1007/s12665-012-1614-2

Noack V, Scheck-Wenderoth M, Cacace M, Schneider M (2013) Influence of moving fluids on the regional thermal field: results from 3D numerical modelling for the area of Brandenburg (North German Basin). Environ Earth Sci. doi:10.1007/s12665-013-2438-4

Norden B, Förster A (2006) Thermal conductivity and radiogenic heat production of sedimentary and magmatic rocks in the Northeast German Basin. AAPG Bull 90(6):939–962

Norden B, Förster A, Balling N (2008) Heat flow and lithospheric thermal regime in the Northeast German Basin. Tectonophysics 460:215–229

Ollinger D, Baujard C, Kohl T, Moeck I (2010) Distribution of thermal conductivities in the Groß Schönebeck (Germany) test site based on 3D inversion of deep well data. Geothermics 39:46–58

Pommer H (2012) The control of faults on the thermal field in Northern Germany—constraints from 2D coupled numerical simulations. Department of Earth Sciences, Freie Universität Berlin, pp 1–69

Przybycin A (2011) Sensitivity study on mesh dependence for 3D coupled fluid- and heat-transport-simulations—an example from the North East German Basin. Department of Earth Sciences, Freie Universität Berlin, pp 1–83

Rawling GC, Goodwin LB, Wilson JL (2001) Internal significance of contrasting fault-zone types. Geology 29:43–46

Reinicke A, Zimmermann G, Huenges E, Burkhardt H (2005) Estimation of hydraulic parameters after stimulation experiments in the geothermal reservoir Groß Schönebeck 3/90 (Norh-German Basin). Int J Rock Mech Min Sci 42:1082–1087

Scheck M (1997) Dreidimensionale Strukturmodellierung des Nordostdeutschen Beckens unter Einbeziehung von Krustenmodellen (Dissertation Thesis, Freie Universität Berlin). Scientific Technical Report STR97/10, GeoForschungsZentrum Potsdam, pp 1–126

Simms MA, Garven G (2004) Thermal convection in faulted 1172 extensional sedimentary basins: theoretical results from finite element modeling. Geofluids 4:109–130

Sippel J, Fuchs S, Cacace M, Kastner O, Huenges E, Scheck-Wenderoth M (2013) Deep 3D thermal modelling for the city of Berlin (Germany). Environ Earth Sci. doi:10.1007/s12665-013-2679-2

Smith L, Forster CB, Evans JP (1990) Interaction between fault zones, fluid flow and heat transfer at the basin scale. In: Newman SP, Neretnieks I (eds) Hydrogeology of Low Permeability Environments. International Association of Hydrological Sciences selected papers in Hydrogeology, vol 2, pp 41–67

Stackebrandt W, Manhenke V (eds) (2002) Atlas zur Geologie von Brandenburg im Maßstab 1:1,000,000. Landesamt für Geowissenschaften und Rohstoffe, Kleinmachnow

Turcotte DL, Schubert G (2002) Geodynamics. Cambidge University Press, New York

Verhoogen J (1980) Energetics of the Earth. National Academy of Sciences, Washington, DC

Yang J (2006) Full 3-D numerical simulation of hydrothermal field flow in faulted sedimentary basins: example of the McArthur Basin, Northern Australia. J Geochem Explor 89:440–444

Zhang X, Sanderson DJ, Barker AJ (2002) Numerical study of fluid flow of deforming fractured rocks using dual porosity permeability model. Geophys J Int 151(2):452–468

Zhang X, Koutsabeloulis N, Heffer K (2007) Hydromechanical modeling of critically stressed and faulted reservoirs. AAPG Bull 91(1):31–50

Zimmermann G, Reinicke A, Blöcher G, Milsch H, Gehrke D, Holl H-G, Moeck I, Brandt W, Saadat A, Huenges E (2007) Well path design and stimulation treatments at the geothermal research well GtGrSk4/05 in Groß Schönebeck. In: Proceedings of thirty-second workshop on geothermal reservoir engineering. Stanford University, Stanford, California, January 22–24, 2007, SGP-TR-183, pp 1–6

Zimmermann G, Moeck I, Blöcher G (2010) Cyclic waterfrac stimulation to develop an enhances geothermal system (EGS)—conceptual design and experimental results. Geothermics 39(1):59–69

Zimmermann G, Blöcher G, Reinicke A, Brandt W (2011) Rock specific hydraulic fracturing and matrix acidizing to enhance a geothermal system—concepts and field results. Tectonophysics 503(1–2):146–154